Title: Competitive Inhibitors of Ras Effector Binding

Authors:

Svenja Wiechmann[1,2], Pierre Maisonneuve[3], Britta M. Grebbin[4,5,6], Meike Hoffmeister[1,7], Manuel Kaulich[1,8], Hans Clevers[9,10,11], Krishnaraj Rajalingam[12], Igor Kurinov[13], Henner F. Farin[4,5,6], Frank Sicheri[3] and Andreas Ernst[1,2,*]

Affiliations:

[1]Institute of Biochemistry II, Goethe University Frankfurt - Medical Faculty, University Hospital, Frankfurt am Main, Germany.

[2]Fraunhofer Institute for Molecular Biology and Applied Ecology IME, Project Group Translational Medicine and Pharmacology TMP, Theodor-Stern-Kai 7, 60590 Frankfurt am Main, Germany.

[3]Lunenfeld-Tanenbaum Research Institute, Sinai Health System, Toronto, ON M5G 1X5, Canada.

[4]German Cancer Consortium (DKTK), 69120 Heidelberg, Germany.

[5]Georg-Speyer-Haus, Institute for Tumor Biology and Experimental Therapy, 60596 Frankfurt am Main, Germany.

[6]German Cancer Research Center (DKFZ), 69120 Heidelberg, Germany.

[7]Institute of Biochemistry, Brandenburg Medical School (MHB) Theodor Fontane, Neuruppin and Brandenburg an der Havel, Germany.

[8]Frankfurt Cancer Institute, Frankfurt am Main, Germany.

[9]Hubrecht Institute, Royal Netherlands Academy of Arts and Sciences (KNAW) and University Medical Center (UMC) Utrecht, Netherlands.

[10]Cancer Genomics Netherlands, UMC Utrecht, Netherlands.

[11]Center for Molecular Medicine, Department of Genetics, UMC Utrecht, Netherlands.

[12]Molecular Signaling Unit-FZI, Institute of Immunology, University Medical Center Mainz, JGU-Mainz, Germany.

[13]Department of Chemistry and Chemical Biology, Cornell University, NE-CAT, Argonne, IL 60439, USA.

[*]Corresponding author: Andreas Ernst (a.ernst@em.uni-frankfurt.de)

Abstract:

The small GTPases H, K and NRas are molecular switches that are indispensable for the correct regulation of cellular proliferation and growth. Mutations in Ras are associated with cancer and result in unwanted activation of signaling processes caused by aberrant recruitment of downstream effector proteins. In this study, we have engineered variants of the Ras-binding domain (RBD) of CRAF kinase that bind with highly improved affinity the effector binding site of Ras. Structural characterization demonstrates how the engineered RBD variants outcompete effector binding and inhibit Ras signaling in cells leading to apoptosis, growth arrest and senescence. The optimized RBD variants provide new insights in Ras biology and enabled the functional stratification of Ras dependency in patient-derived colorectal cancer organoids.

One sentence summary:

Inhibition of effector kinase binding to Ras induces senescence in non-tumorigenic cells and reveals Ras dependency in patient-derived cancer organoids.

Main Text:

The small GTPases H, K and NRas are molecular switches that regulate the relay of signals from growth factor receptor tyrosine kinases to transcription factors effecting the growth and proliferation of cells. To achieve this signal relay, Ras GTPases cycle their protein conformation between an inactive, guanosine 5'-diphosphate (GDP)-bound state and an active, guanosine 5'-triphosphate (GTP)-bound state that binds downstream effector proteins. Along this reaction cycle, the weak hydrolysis-activity of Ras is enhanced by GTPase activating proteins (GAPs), while guanine exchange factors (GEFs) facilitate the discharge of GDP and the reloading with GTP. In cancer, mutations in Ras shift the fine-tuned equilibrium of this reaction cycle to the active, GTP-bound state resulting in a constitutive activation of downstream kinases. This uncouples the regulatory link between proliferation and upstream receptor signaling resulting in uncontrolled growth and proliferation. Thus, mutated Ras GTPases have a prominent role as oncogenic driver in various malignancies making them a major focus for the development of anti-proliferative drugs. However, due to the high affinity of guanosine di/tri-phosphate (GDP/GTP) to Ras and due to the flat topology of the effector binding site only a few small molecule inhibitors exist to date that directly interfere with Ras function [1]. To overcome the paucity of small molecules that directly interfere with Ras activity, several affinity reagents based on protein scaffolds have been developed to address different facets of Ras biology. For example, fibronectin derived monobodies were shown to inhibit signaling by disrupting dimerization of H and KRas at the plasma membrane [2], thereby supporting earlier studies, which described nano-clustering of 6 - 7 Ras molecules as a prerequisite for effector recruitment [3, 4]. Also, it has recently been shown that interfering with Ras dimerization limits the growth of xenografts that inducibly express the monobody [5]. An alternative, more direct strategy for inhibiting Ras-signaling using engineered proteins is to prevent the recruitment of downstream effectors or block the activation of Ras by GEFs. To this end, several affinity reagents have been generated that compete with Ras effectors by selectively binding to the active or inactive state of Ras [6, 7, 8, 9, 10, 11, 12]. Interestingly, recent work showed that a subset of these affinity reagents had only effects in cells at high concentrations [9, 10, 13]. This partial success provides a rationale for affinity reagents with improved efficacy.

An ideal affinity reagent to inhibit Ras-function should avoid steric constraints by precisely replicating effector binding to activated, GTP-bound Ras. Additionally, these affinity

reagents should have a high affinity to the effector binding site and outcompete downstream effectors. Consequently, such an affinity reagent would act as inhibitor of Ras signaling that allows to probe the biology of Ras inhibition in cellular and patient-derived model systems. To derive an affinity reagent that fulfills these criteria, we adapted our strategy of optimizing pre-existing intermolecular contacts [14, 15] to the Ras-binding domain (RBD) of the CRAF kinase. We constructed a phage-displayed RBD library encoding mutations of interface residues and selected for improved binding to active, GTP-bound Ras. Crystal structures of complexes with activated Ras showed that the RBD variants precisely mimic effector binding and the engineered mutations subtly improve intermolecular contacts. Importantly, intracellular expression of the RBD variants results in growth reduction, apoptosis and senescence in various cell lines due to a robust inhibition of Ras signaling and the MAP kinase signaling cascade. Finally, in patient-derived organoids, we show that the RBD variants led to a reduced cellular activity and growth, thereby elucidating the Ras dependency of colorectal tumor organoids.

Engineered RBDvs have improved affinity and compete with effector binding *in vitro*

Previous studies demonstrated that the CRAF-RBD is highly tolerant to mutations and can be computationally engineered to preferentially bind inactive states of Ras [11, 16, 17]. In order to optimize the interface of the RBD to active Ras, we analyzed existing crystal structures of Ras:RBD complexes [18, 19, 20], eventually randomizing 14 surface-exposed RBD residues that are in contact or in close proximity to the effector binding site (**Fig. 1A**). Additionally, we replaced three unpaired cysteines at position 81, 95 and 96 of the RBD with serine residues to prevent dimerization of phage-displayed proteins and improve overall display of the RBD variants. Our final library contained more than $2x10^9$ unique RBD variants (RBDvs) presented on the surface of filamentous phage and subsequent selection by phage display yielded 5 variants with improved binding to surface immobilized GTPγS-loaded HRas (**Fig. 1B**). The replacement of the three surface exposed cysteine residues proved to be a prerequisite for the positive outcome of the selection experiment. The selected variants show a conserved mutational pattern indicating a shared binding mode to activated Ras. Strikingly, the mutation Gln^{66} to Glu and the previously identified Val^{88} to Arg mutation that has been shown to increase affinity of the RBD to HRas [21] are conserved amongst all 5 variants. Additionally, we found that an Arg^{89} to His mutation is highly enriched and occurs in four out

of five RBDvs. After purification as His-tagged proteins, we tested if the engineered RBDvs were able to outcompete CRAF-RBDwt binding to GTPγS-loaded KRas *in vitro* (**Fig. 1C**). Relative to RBDwt control, all engineered variants showed an improved ability to compete off GTPγS KRas in solution. A similar competitive potential of the RBDvs was observed using the RalGDS-Ras association domain (RA) instead of the CRAF-RBDwt as bait protein (**Supplementary Fig. 1A**). As RBDv1 and RBDv12 performed best in these experiments, we focused our further analysis on these two variants. Affinity measurements confirmed that the two variants have improved binding properties relative to RBDwt for activated HRas with K_ds of about 3 nM versus 63 nM (**Fig. 1D and Fig. 1E**). In control experiments, we confirmed that His-tagged HRas GTPγs does not bind to GST-loaded sensors or empty sensors alone (**Supplementary Fig. 1B**) indicating that the slow off rate is not due unspecific binding of HRas to GST or the sensor material. Importantly, the variants were selective for activated HRas and did not bind GDP-loaded HRas (**Supplementary Fig. 1C**).

The engineered RBDvs mimic effector binding to active Ras

To understand the structural basis for improved binding, we crystallized HRas G12V in complex with RBDv1 at 2.9 Å and RBDv12 at 3.15 Å resolution (**Fig. 2A and Supplementary Table 1**). Structural analysis revealed that the RBDvs engaged the effector binding site of HRas through a canonical binding mode [20] with only minor shifts to the center of mass positions and rotation angle (1.8 Å/15˚ and 2.0 Å/16˚ for RBDv1 and RBDv12, respectively). Similar to the canonical binding mode of RBDwt, the β2 of the RBDvs form an extended intermolecular β-sheet with the β2 of HRas (**Supplementary Fig. 2A**). In addition, helices α1 of both RBDwt and RBDvs form direct contacts with switch 1 residues in Ras (**Supplementary Fig. 2B**). Inspection of direct contact interface reveals that the conserved RBDvs-mutations Gln^{66} to Glu, Val^{88} to Arg and Arg^{89} to His result in a rewiring of the hydrogen (H)-bonding pattern to the Asp^{38} and Tyr^{40} side chains in HRas (**Fig. 2B**). This change in H-bonding pattern together with steric effects involving Ile^{21} in HRas and Val^{88} to Arg in RBDvs appears to be responsible for a shift of the α1-helix of the RBDvs relative to that observed in RBDwt (**Fig. 2A and Supplementary Fig. 2B**). As the binding mode of RBDvs to HRas overlaps completely with RBDwt, the RBDvs are expected to act as competitive inhibitor of all Ras effectors which engage this common binding site.

RBDvs are highly specific for the active conformation of the effector binding site in Ras GTPases

We next tested the intracellular specificity of the RBD variants using mass spectrometry. Hemagglutinin (HA)-tagged RBDvs and RBDwt control were inducibly expressed in stably transduced colon carcinoma HCT 116 cells and HA-immunoprecipitated (**Fig. 3A and Supplementary Fig. 3A**). Strikingly, RBDv1 and RBDv12 displayed up to 5500-fold enrichment of peptides originating from endogenous KRas G13D relative to RBDwt indicating that the variants preferentially bind constitutively active oncogenic Ras in HCT 116 cells (**Fig. 3B**). Additionally, we identified to a 10-fold lesser extent peptides of other Ras-subfamily GTPases that share conserved effector binding sites (**Fig. 3B and C, Supplementary Table 2)**. This finding demonstrates that the RBDvs bind to their intended target in cells and thus have the potential to block downstream effectors for binding to activated Ras and to act as inhibitors of Ras-mediated signaling processes in cells. Importantly, the observed high enrichment factor underlines the preferred incidence of KRas G13D in a constitutively active, GTP-bound state in HCT 116 cells.

RBDvs inhibit activation of ERK and AKT pathways resulting in reduced metabolic activity and apoptosis

To test if the RBDvs act as inhibitors of Ras signaling processes, we probed whole cell lysates from HCT 116 cells expressing HA-tagged RBDvs and RBDwt-control with antibodies detecting the phosphorylation state of Ras downstream kinases. A comparable analysis was conducted with transduced immortalized retinal pigmented epithelium (hTERT RPE1) cells [22] to understand how non-tumorigenic cells respond to Ras inhibition. Immunoblot analysis confirmed that the RBDvs reduced the phosphorylation of the growth signal activated protein kinases MEK1/2 and ERK1/2 in HCT 116 and RPE1 cells (**Fig. 4A**). The corresponding control experiments with RBDwt, despite its higher expression level, did not show any reduction of MAP kinase phosphorylation demonstrating that the improved affinity of the RBDvs to active Ras isoforms is required to suppress activation of downstream kinases. Interestingly, HCT 116 cells but not RPE1 cells respond with a reduced phosphorylation of Ser^{473} in the serine/threonine kinase AKT (**Fig. 4B**). This suggests that the two cell lines diverge in signaling downstream of Ras. The observation that RPE1 cells do not show

reduced AKT phosphorylation is most likely due to a Ras-independent regulation of PI3K activation in full medium.

To address the differing behavior of RPE1 cells in full medium, we repeated these experiments in serum-starved cells treated with epidermal growth factor (EGF) to stimulate upstream Ras activation. In these experiments, the expression of the RBDvs in RPE1 cells led to reduced ERK1/2 and AKT phosphorylation demonstrating that the RBDvs inhibit both signaling pathways under these conditions (**Fig. 4C**). Thus, this observation in non-tumorigenic cell lines suggests that depending on the availability of growth factors the activation of the PI3K pathway bypasses Ras-mediated signaling.

Next, we asked if the reduced activity of MAP kinase pathway translates to an effect on the metabolic rate by detecting the ATP content in the corresponding cell lines (**Fig. 4D**). In HCT 116 and RPE1 cells, the ATP content was reduced demonstrating that inhibition of effector binding to active Ras by the RBDvs reduces the metabolic rate. The RPE1 cells responded under these experimental conditions with up to 80% reduction of cellular activity in the presence of the RBDvs. Additionally, we confirmed these results by measuring growth curves for both cell lines (**Supplementary Fig. 3B**). Furthermore, expression of the inhibitory RBDvs in MIA PaCa-2 (KRas G12C), A549 (KRas G12S) and H1299 (NRas Q61K) cancer cell lines results in reduced ERK phosphorylation and also to a reduced metabolic rate, indicating that the RBDvs are a general tool to disrupt Ras signaling in cell lines from different cancer backgrounds (**Supplementary Fig 3C and D**).

In a next step, we asked if the reduced cellular activity in HCT 116 and RPE1 cell lines is due to an increased incidence of apoptosis (**Fig. 4E and Supplementary Fig. 4A**). Quantification of flow cytometry data of annexin V staining revealed that in the presence of the inhibitory RBDvs both cell lines responded differently in full medium: while HCT 116 cells have an up to 2.7-fold increased number of apoptotic cells compared to non-induced controls, RPE1 cells show no sign of apoptosis under these conditions (**Fig. 4E**). Earlier studies described that simultaneous inhibition of MAP and PI3 kinase pathways in HCT 116 cells is required to induce apoptosis [23]. Here, however, this result is corroborated by using our engineered site-specific Ras inhibitors to block effector binding to active Ras. Subsequently, we tested in serum-starvation condition if the simultaneous inhibition of PI3K and ERK signaling induces apoptosis in RPE1 cells. Indeed, when deprived of growth factors, RPE1 cells show an up to 7-fold increased incidence of apoptotic cells relative to the RBDwt

control in the presence of the inhibitory RBDvs (**Fig. 4F and Supplementary Fig. 4B)** indicating that, analogous to HCT 116 cells, inhibition of both pathways is required to induce apoptosis. Nevertheless, the absence of apoptosis in RPE1 cells in full medium conditions does not explain the reduced metabolic rate and the decelerated growth that we have observed before (**Fig. 4D and Supplementary Fig. 3B**).

RBDvs-mediated inhibition of Ras signaling leads to senescence in retinal pigmented epithelial cells

To address this question, we asked if Ras inhibition by the RBDvs has an effect on cell cycle progression (**Fig. 5A and Supplementary Fig. 5A**). Flow cytometry of bromodeoxyuridine (BrdU)/propidium iodide (PI) stained cells showed that in the presence of the RBDvs the RPE1 cells are predominantly in G1/G0 phase, while S phase is significantly reduced. Importantly, RPE1 cells expressing RBDwt control progress normally through the cell cycle indicating that the G1/G0 arrest is due to the inhibition of effector binding to Ras. In contrast, HCT 116 cells are distributed evenly over all stages of the cell cycle most likely due to the reported mutation of cyclin dependent kinase inhibitor 2A ($p16^{INK4a}$) that suppresses control of S-phase entry at the restriction point in G1-phase [24]. In order to elucidate the biochemical details of the cell cycle arrest, we probed the corresponding cell lysates of RPE1 and HCT 116 cells for the levels of different cell cycle regulated proteins. Since the HCT 116 cells do not show any changes in cell cycle progression, we included them as a negative control in this analysis. Interestingly, immunoblot of lysates from RPE1 cells showed no phosphorylation of retinoblastoma protein (pRb) and an overall reduced amount of pRb in the presence of the inhibitory RBDvs (**Fig. 5B**). For normal cell cycle progression to occur, pRb is phosphorylated thereby releasing transcriptional suppression of cell cycle proteins such as cyclin D1 and cyclin dependent kinases (CDK) 2 and 4; this results in a feed forward hyper-phosphorylation of pRb resulting in G1-restriction point release followed by S-phase entry [25]. Consequently, the reduced phosphorylation of pRb is potentially caused by a diminished feed forward activity of cell cycle kinases indicated by the decreased CDK2 and cyclin D1 levels. The observation that the levels of the CDK4/6 inhibitors p16 and p21 are unaffected in the presence of RBDvs and RBDwt controls indicates that the cell cycle arrest is independent from a p53-mediated stress response [26]. As expected, HCT 116 cells do not show any changes in cell cycle proteins in presence or absence of the RBDvs. Importantly, in

non-induced RPE1 cells, the cell cycle proteins are not affected indicating that the reduction of pRb and CDK2 levels is due to the inhibition of Ras signaling by the high affinity RBDvs. Since these findings on the molecular level suggest that the RPE1 cells respond with cell cycle exit, we probed the cells for the presence of senescence-associated (SA)-β-galactosidase. Indeed, within 24 h after induction of the RBDvs, RPE1 cells undergo senescent-associated morphological changes and are positive for SA-β-galactosidase (**Fig. 5C**). In doxycycline wash-out experiments, we confirmed that the RPE1 cells remain SA-β-galactosidase positive and have permanently left the cell cycle (**Supplementary Fig. 5B**). Quantification of flow cytometry data confirms that within 48 h of inhibiting Ras signaling, almost 50% of the RPE1 cells are senescent (**Fig. 5D and Supplementary Fig. 5C**). Importantly, under these experimental conditions, the expression of the negative control RBDwt does not induce senescence showing that the cell cycle exit of RPE1 cells is due to the inhibition of Ras signaling by the RBDvs.

RBDvs lead to reduced growth in patient-derived colorectal cancer organoids

To investigate whether the characteristics of our RBDvs in cell culture can be translated into a patient-derived model, we used tumor organoids with known Ras mutation status isolated from surgically removed colorectal carcinoma from 7 patients [27] (**Supplementary Table 3**). After transduction with the doxycycline-inducible lentiviral constructs, we compared cell viability and growth of organoids expressing RBDvs or RBDwt cultured in Matrigel. We first confirmed by immunoblot of lysates from the organoids that ERK and AKT phosphorylation is suppressed in response to doxycycline-induced expression of the RBDvs (**Fig. 6A**). In the mutant Ras organoids P6T and P28T, and the Ras wt organoids P17T and P24bT, we observed a suppression of metabolic activity as indicated by the cellular ATP content (**Fig. 6B**). In addition, the effect of RBDvs on cell viability correlated well with decreased colony size as determined by bright field microscopy (**Fig. 6C**). The quantification of the colony size indicates that in the presence of the inhibitory RBDvs the reduced growth is significant compared to non-induced organoids (**Fig. 6D**). Thus, this result provides evidence that inhibition of Ras signaling by the RBDvs leads to a growth disadvantage of various patient-derived colon cancer cell lines. Moreover, our experiments revealed that not all transduced organoids react equally well to the inhibition of Ras signaling **(Supplementary Fig. 6)**, and thus the RBDvs facilitate a functional classification of Ras dependency of colorectal cancer

samples. A downstream activation of growth signaling by mutant BRAF or PI3K in these organoids can be ruled out because in our analysis we have selected organoids that are BRAF and PI3K wild type [27] (**Supplementary Table 3**). In conclusion, the RBDvs successfully decrease the growth of four patient-derived organoid lines indicating that inhibiting Ras-effector binding to activated Ras may be a valid strategy in cancer therapy.

Discussion

By engineering the Ras-Raf interface of the CRAF-RBD, we were able to develop potent and highly selective Ras inhibitors that outcompete the binding of signaling effectors to activated Ras. The engineered variants selectively bind Ras in an active conformation by establishing contacts to a minimal epitope composed of switch 1 residues at the center of the effector binding site. High affinity is achieved by a subtle rewiring and optimization of the hydrogen bond pattern at the interface between RBD and HRas. Since the effector binding site is conserved amongst Ras-family members, we detected in coupled Co-IP/MS experiments also other Ras GTPases with a nearly identical sequence composition in the switch 1 region interacting with the RBDvs. Nevertheless, the mutant form KRas G13D is strongly enriched in Co-IPs from HCT 116 cells indicating that the RBDvs preferentially bind constitutively active Ras GTPases in cells. In intracellular experiments, expression of RBDvs efficiently downregulated ERK and AKT phosphorylation resulting in a decelerated cellular growth or induction of apoptosis in several cell lines from different cancer backgrounds. Interestingly, in the presence of growth factors, non-tumorigenic RPE1 cells expressing the Ras inhibitors become senescent within 24 to 48 hours. In these cells and under full medium conditions, we detect a reduction of ERK phosphorylation while AKT phosphorylation is maintained. Thus, Ras inhibition by the RBDvs results in an imbalance between both pathways that causes an oncogene-induced senescence-like phenotype. Whether the observed imbalance between the two proliferative signaling pathways in the presence of selective Ras inhibitors is due to negative feedback loops or orthogonal, Ras-independent activation of the PI3K signaling pathway is currently unclear. The latter is suggested by the observation that the decision between a senescent and an apoptotic phenotype seems to depend on the presence of growth factors: in serum-depleted RPE1 cells, we observed a concomitant inhibition of AKT and ERK phosphorylation, which eventually led to apoptosis.

In order to apply these results to a clinical research question, we asked if the RBDvs could be used as a tool to delineate Ras dependency in colorectal cancer carcinoma (CRC) [27].

In CRC a number of different signaling pathways have been implicated in the pathogenesis of the disease [28]. However, the extent and heterogeneity of genetic alterations in CRC makes it difficult to analyze the contribution of individual metabolic pathways to the proliferative phenotype [27]. Consequently, there is great interest in elucidating the role of, for example, the Ras signaling pathway for the proliferation of CRC. In our experiments, we showed that the inhibition observed in adherent cell culture experiments translates to patient-derived colorectal cancer organoids resulting in reduced growth of several organoids. Indicative of their varying degree of Ras dependency, not all organoids responded equally well to Ras inhibition by the inhibitory RBDvs, demonstrating that the RBDvs facilitate a functional classification of Ras dependency in intestinal tumor organoids.

Although the RBDvs are a unique tool for studying Ras-dependent signaling processes, several intracellular affinity reagents targeting GTP-bound Ras have recently been published [6, 8, 9, 10]. This raises the question of how the RBDvs compare to these engineered proteins. For example, the affinity reagent R11.1.6, based on a DNA-binding domain from a thermophilic archaeon, was engineered to bind Ras in an active conformation and was shown to compete with effector binding [8]. Although initial experiments in HEK293T cells suggested otherwise, surprisingly, R11.1.6 did not affect Ras-mediated signaling in a broad range of cancer cell lines [13]. Kauke et al. concluded that a higher concentration of R11.1.6 is required to efficiently outcompete Ras-binding effectors. Similar observations have been made using intracellular antibodies targeting the Ras-effector binding interface. In case of the antibody fragment iDab#6, a membrane localization peptide was required to overcome the binding avidity of Ras-effectors and to inhibit Ras-dependent signaling events [9]. The cell penetrating TMab4 RT11 antibody targeting the switch 1 site of Ras family GTPases has also been described to require high concentrations to effectively inhibit Ras-mediated signaling events. Whether this observation is due to a comparable avidity effect or incomplete release of the antibody from the endosomes is unclear [10]. In addition to these examples, two designed ankyrin repeat proteins (DARPins) with specificity to either the GDP-bound inactive state (K27) or the GTP-bound active state (K55) of Ras have recently been reported [6]. Both DARPins inhibit Ras signaling, however, it remains to be seen if the observed effects also translate to other cell types and organoids. A comparison of the reported affinities of K55 with 167 nM and CRAF-RBDwt with ~ 60-80 nM for GTP-bound Ras also suggests that a high concentration is required for the observed competition of K55 with CRAF-RBDwt and other

downstream effector proteins. In contrast to these reports, the intracellular inhibition of Ras signaling by the RBDvs does not show comparable avidity effects. Indeed, we observed robust inhibition in several different cell lines despite the fact that expression of the RBDvs is always lower than the corresponding wt-control. Thus, by mimicking their natural binding mode, but with higher affinity, the RBDvs efficiently compete with downstream Ras-binding effector kinases. The structural accuracy of RBDvs binding to the Switch 1 region of activated Ras therefore makes them a highly specific, dominant-negative intracellular affinity reagent, which represents an alternative to decode Ras-dependent signaling processes.

In addition to the affinity reagents that interact with active Ras GTPases, several reagents have been developed that prevent signaling by stabilizing an inactive state of Ras or targeting Ras binding domains directly [7, 12, 29]. For example, a cell permeable bicyclic peptide was developed that competes with RBD-binding at a moderate IC_{50} of 3.4 μM *in vitro* [12]. However, the peptide has a two-fold higher preference to bind the inactive state of Ras, making it unclear whether the observed inhibition of the MAP and PI3K kinase pathway is due to inhibition of nucleotide exchange or competition with downstream kinases. Moreover, a pico-molar affinity reagent was engineered using yeast display, which causes a structural rearrangement of the switch 1 region, exposing the GDP/GTP binding site in Ras [7]. However, the presence of a disulfide bridge precludes its use as a tool-compound to target Ras in cells. Additionally, the induced structural changes in Ras result in a new binding interface that is independent of the activation status of Ras. An alternative strategy to targeting Ras GTPase is to create compounds that prevent binding of downstream kinases by blocking the binding interface of RBDs itself. For example, the small molecule rigosertib has been described to bind to the RBD of Raf kinases and block Ras signaling [29]. However, recent research has revealed that rigosertib preferentially interacts with β-tubulin indicating that the compound lacks specificity for the RBD-interface [30]. Consequently, the non-specific interactions of rigosertib makes it difficult to interpret if the observed phenotypes are due to inhibition of downstream kinase binding or other off-target effects. In contrast, the RBDvs are highly specific for active Ras and the observed phenotypes are consistent with an inhibition of downstream kinase activation. Thus, the RBDvs are a unique molecular tool to study and decode the network of Ras-mediated signaling events in cell lines and also in patient-derived model systems. Finally, the RBDvs allow the evaluation of phenotypic

consequences of Ras inhibition in a wider context potentially paving the way for the development of drugs targeting Ras-effector binding.

References and Notes:

1. Cox AD, Fesik SW, Kimmelman AC, Luo J, Der CJ. Drugging the undruggable RAS: Mission possible? *Nat Rev Drug Discov* **13**, 828-851 (2014).

2. Spencer-Smith R*, et al.* Inhibition of RAS function through targeting an allosteric regulatory site. *Nat Chem Biol* **13**, 62-68 (2017).

3. Plowman SJ, Muncke C, Parton RG, Hancock JF. H-ras, K-ras, and inner plasma membrane raft proteins operate in nanoclusters with differential dependence on the actin cytoskeleton. *Proc Natl Acad Sci U S A* **102**, 15500-15505 (2005).

4. Zhou Y*, et al.* SIGNAL TRANSDUCTION. Membrane potential modulates plasma membrane phospholipid dynamics and K-Ras signaling. *Science* **349**, 873-876 (2015).

5. Khan I, Spencer-Smith R, O'Bryan JP. Targeting the alpha4-alpha5 dimerization interface of K-RAS inhibits tumor formation in vivo. *Oncogene*, (2018).

6. Guillard S*, et al.* Structural and functional characterization of a DARPin which inhibits Ras nucleotide exchange. *Nat Commun* **8**, 16111 (2017).

7. McGee JH*, et al.* Exceptionally high-affinity Ras binders that remodel its effector domain. *J Biol Chem* **293**, 3265-3280 (2018).

8. Kauke MJ*, et al.* An engineered protein antagonist of K-Ras/B-Raf interaction. *Sci Rep* **7**, 5831 (2017).

9. Tanaka T, Williams RL, Rabbitts TH. Tumour prevention by a single antibody domain targeting the interaction of signal transduction proteins with RAS. *EMBO J* **26**, 3250-3259 (2007).

10. Shin SM*, et al.* Antibody targeting intracellular oncogenic Ras mutants exerts anti-tumour effects after systemic administration. *Nat Commun* **8**, 15090 (2017).

11. Filchtinski D, Sharabi O, Ruppel A, Vetter IR, Herrmann C, Shifman JM. What makes Ras an efficient molecular switch: a computational, biophysical, and structural study of Ras-GDP interactions with mutants of Raf. *J Mol Biol* **399**, 422-435 (2010).

12. Trinh TB, Upadhyaya P, Qian Z, Pei D. Discovery of a Direct Ras Inhibitor by Screening a Combinatorial Library of Cell-Permeable Bicyclic Peptides. *ACS Comb Sci* **18**, 75-85 (2016).

13. Kauke MJ, Tisdale AW, Kelly RL, Braun CJ, Hemann MT, Wittrup KD. A Raf-competitive K-Ras binder can fail to functionally antagonize signaling. *Mol Cancer Ther*, (2018).

14. Ernst A*, et al.* A strategy for modulation of enzymes in the ubiquitin system. *Science* **339**, 590-595 (2013).

15. Wiechmann S*, et al.* Site-specific inhibition of the small ubiquitin-like modifier (SUMO)-conjugating enzyme Ubc9 selectively impairs SUMO chain formation. *J Biol Chem* **292**, 15340-15351 (2017).

16. Campbell-Valois FX, Tarassov K, Michnick SW. Massive sequence perturbation of a small protein. *Proc Natl Acad Sci U S A* **102**, 14988-14993 (2005).

17. Kiel C, Filchtinski D, Spoerner M, Schreiber G, Kalbitzer HR, Herrmann C. Improved binding of raf to Ras.GDP is correlated with biological activity. *J Biol Chem* **284**, 31893-31902 (2009).

18. Erijman A, Shifman JM. RAS/Effector Interactions from Structural and Biophysical Perspective. *Mini Rev Med Chem* **16**, 370-375 (2016).

19. Kiel C, Serrano L, Herrmann C. A detailed thermodynamic analysis of ras/effector complex interfaces. *J Mol Biol* **340**, 1039-1058 (2004).

20. Fetics SK*, et al.* Allosteric effects of the oncogenic RasQ61L mutant on Raf-RBD. *Structure* **23**, 505-516 (2015).

21. Fridman M*, et al.* Point mutants of c-raf-1 RBD with elevated binding to v-Ha-Ras. *J Biol Chem* **275**, 30363-30371 (2000).

22. Bodnar AG*, et al.* Extension of life-span by introduction of telomerase into normal human cells. *Science* **279**, 349-352 (1998).

23. Wee S*, et al.* PI3K pathway activation mediates resistance to MEK inhibitors in KRAS mutant cancers. *Cancer Res* **69**, 4286-4293 (2009).

24. Okamoto A*, et al.* Mutations and altered expression of p16INK4 in human cancer. *Proc Natl Acad Sci U S A* **91**, 11045-11049 (1994).

25. Narasimha AM, Kaulich M, Shapiro GS, Choi YJ, Sicinski P, Dowdy SF. Cyclin D activates the Rb tumor suppressor by mono-phosphorylation. *Elife* **3**, (2014).

26. Li J, Poi MJ, Tsai MD. Regulatory mechanisms of tumor suppressor P16(INK4A) and their relevance to cancer. *Biochemistry* **50**, 5566-5582 (2011).

27. van de Wetering M*, et al.* Prospective derivation of a living organoid biobank of colorectal cancer patients. *Cell* **161**, 933-945 (2015).

28. Fearon ER. Molecular genetics of colorectal cancer. *Annu Rev Pathol* **6**, 479-507 (2011).

29. Athuluri-Divakar SK*, et al.* A Small Molecule RAS-Mimetic Disrupts RAS Association with Effector Proteins to Block Signaling. *Cell* **165**, 643-655 (2016).

30. Jost M*, et al.* Combined CRISPRi/a-Based Chemical Genetic Screens Reveal that Rigosertib Is a Microtubule-Destabilizing Agent. *Mol Cell* **68**, 210-223 e216 (2017).

31. Soding J. Protein homology detection by HMM-HMM comparison. *Bioinformatics* **21**, 951-960 (2005).

Acknowledgments:

This work was supported by LOEWE Ub-Net, Cluster of Excellence "Macromolecular Complexes" (DFG EXC115), and the Collaborative Research Center SFB 1177. We thank Mani Ravichandran from the Structural and Genomic Consortium (SGC) of Toronto for providing X-Ray crystallography screening kits. This work was supported by funds from an Impact Grant (704116 to F.S.) from the Canadian Cancer Society Research Institute and by operating funds (FDN143277 to F.S.) from the Canadian Institutes for Health Research. P.M. was supported by a TD Bank postdoctoral fellowship. F.S. holds a Canada Research Chair (Tier 1) in Structural Biology of Cell Signaling. K.R. is a Heisenberg professor of the DFG (RA1739/4-2). Diffraction work conducted at the Northeastern Collaborative Access Team beamlines was funded by the National Institute of General Medical Sciences from the National Institutes of Health (P41 GM103403) and by an NIH-ORIP HEI grant (S10 RR029205).

Author contributions:

S.W. and A.E. designed the study, designed the RBD library, analyzed the data and wrote the manuscript. S.W. performed library construction and selection, *in vitro* competition experiments, binding experiments and all cellular experiments. P.M and I.K. performed structural studies and P.M., F.S., S.W. and A.E. analyzed structural data. S.W. performed Co-IP and MS and S.W., M.H. and A.E. analyzed MS data. K.R. contributed to the design, provided reagents and analyzed data. M.B.G. performed organoid experiments and M.B.G., H.F.F., S.W., H.C. and A.E. analyzed organoid data. M.K. analyzed cell cycle assays and provided reagents.

Competing financial Interest:

None.

Data and materials availability:

All data is available in the main text or the supplementary materials. All data and material will be made available upon request.

Supplementary Materials:

Methods

Supplementary Figures 1-6

Supplementary Tables 1 – 3

References 32 – 50

Figures:

Figure 1

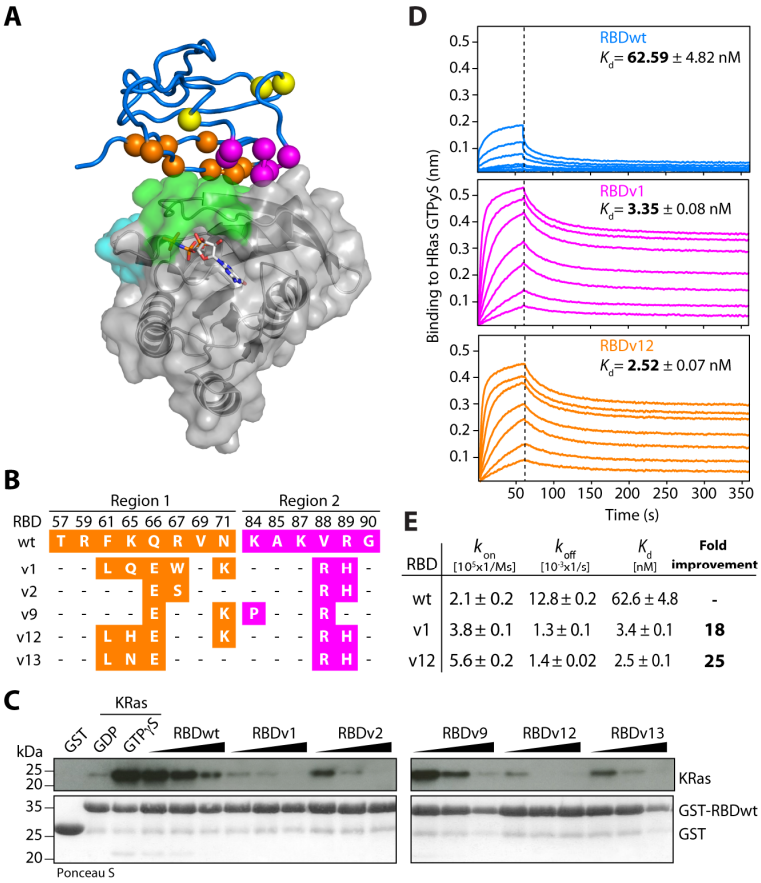

Fig. 1. CRAF-Ras-binding domain (RBD) library design and selected RBD variants (RBDvs) outcompete RBDwt by binding with highly improved affinity to Ras. (**A**) CRAF-RBD in complex with HRas (pdb: 4G0N) [20]. The RBD is shown as blue tube and HRas as transparent surface representation indicating the location of switch 1 (green) and switch 2 (cyan). Residues modified in region 1 (orange), region 2 (magenta) and Cys to Ser mutations (yellow) of CRAF-RBD are shown as colored spheres. (**B**) Sequences of RBDvs selected by phage display. Residues in region 1 and region 2 are colored as in (A). Non-mutated positions are indicated by dashes. (**C**) *In vitro* competition of His-tagged GTPγS-loaded KRas binding to GST-tagged RBDwt immobilized on glutathione sepharose resin with increasing molar ratios of His-tagged RBDvs or RBDwt (1:1, 1:2.5 and 1:10). KRas bound to beads was detected by immunoblot and the corresponding Ponceau S stained membrane is shown. (**D**) Binding of GTPγS-loaded HRas to immobilized GST-tagged RBDwt (blue), RBDv1 (magenta) or RBDv12 (orange) measured by bio-layer interferometry (BLI). Concentrations of Ras ranged from 1 µM to 15.6 nM in a 1:1 dilution series. K_d values for each experiment are shown. (**E**) Binding

constants for the BLI measurements from (D). Values for on rate (k_{on} [10^5x1/Ms]), off rate (k_{off} [10^{-3}x1/s]), dissociation constant (K_d [nM]) and fold improvement are shown.

Figure 2

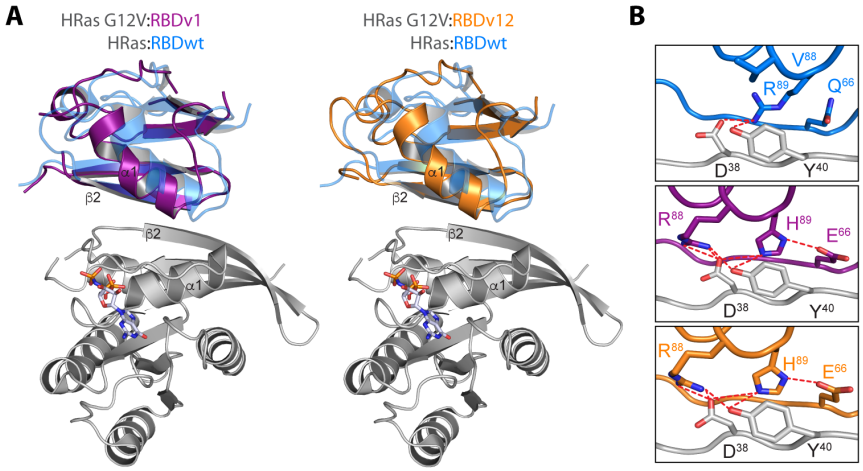

Fig. 2. RBDvs bind at the Ras effector binding site. (**A**) Crystal structures of HRas G12V (grey) in complex with RBDv1 (magenta) at 2.9 Å or RBDv12 (orange) at 3.15 Å resolution. Both structures are superimposed on HRas in complex with RBDwt (blue) (pdb:4G0N) [20]. For clarity, only HRas G12V and the GTP analog phosphoaminophosphonic acid-guanylate ester (GNP) is shown as colored sticks. (**B**) Side by side comparison of HRas in complex with RBDwt (upper panel), RBDv1 (middle panel) or RBDv12 (lower panel) showing changes caused by mutations at positions 66, 88 and 89. Polar interactions are indicated by dashed lines (red). HRas G12V, RBDwt, RBDv1 and v12 main and side chains are colored as in (A). Residues are numbered according to the PDB entry for 4G0N.

Figure 3

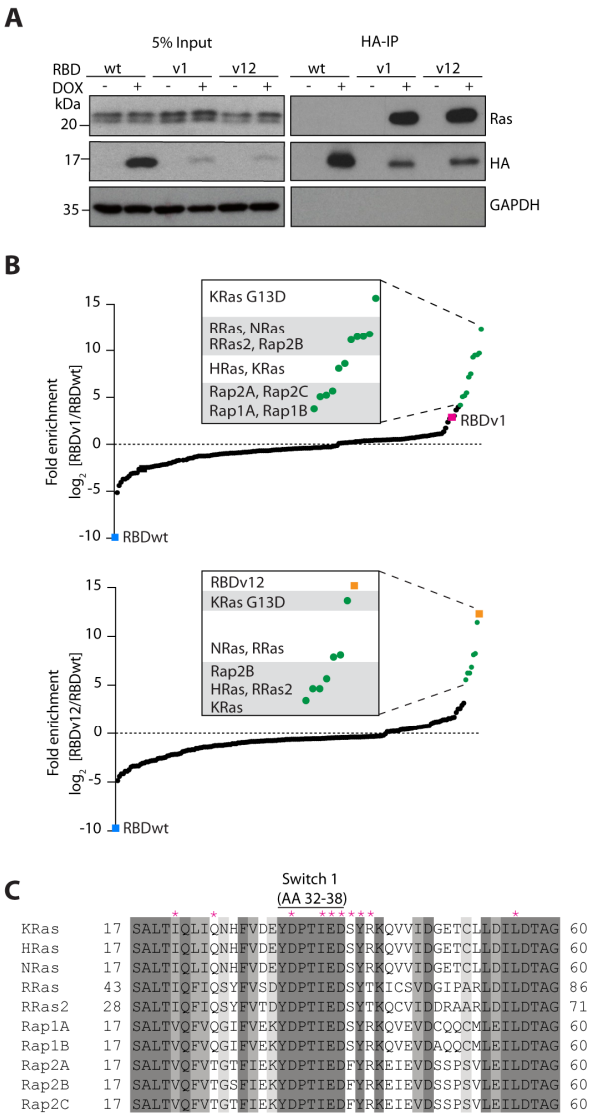

Fig. 3. RBDvs are specifically binding to endogenous KRas G13D in HCT 116 cells. (**A**) Western blot of co-immunoprecipitation using anti-HA beads from lentiviral transduced HCT 116 cells stably expressing HA-tagged RBDwt, RBDv1 and RBDv12 upon induction with doxycycline (DOX) (1 µg/ml, 24h) using the indicated antibodies. (**B**) Mass spectrometry of co-immunoprecipitation samples used in (A). Proteins are ranked according their fold enrichment shown as $\log_2$ ratio for RBDv1 (upper panel) or RBDv12 (lower panel) compared to RBDwt. Only proteins that have been identified with a p-value < 0.05 are shown (n=2). Insets highlight proteins that have been enriched more than 16-fold ($\log_2 > 4$). (**C**) Sequence alignment of Ras GTPases that have been enriched more than 16-fold ($\log_2 > 4$). Conservation of amino acids is highlighted in grey scale (fully conserved residues: dark grey; conservation of amino acids with strongly similar properties: grey; residues with weakly

similar properties: light grey). Magenta asterisks indicate HRas residues within 4.5 Å of RBDvs. Sequence alignment was done using the clustal-omega algorithm [31].

Figure 4

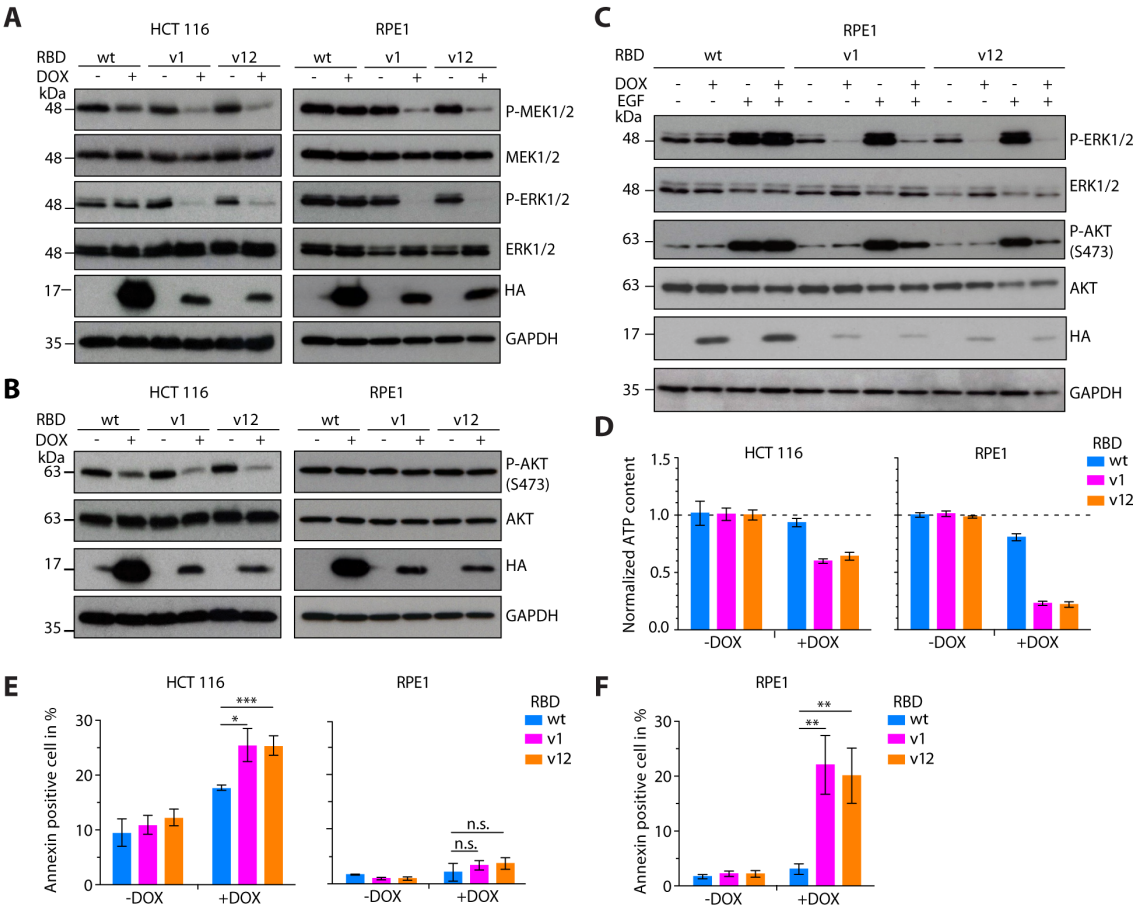

Fig. 4. RBDvs inhibit MAPK and PI3K signaling, reduce cellular viability and induce apoptosis in HCT 116 and RPE1 cells. (**A+B**) Immunoblot of whole cell lysates from HCT 116 and RPE1 cell lines stably transduced with inducible lentiviral constructs expressing HA-tagged RBDwt, RBDv1 or RBDv12 in absence (-) and presence (+) of DOX (1 µg/ml, 24 h). Cell lysates were analyzed using the indicated antibodies. (**C**) Immunoblot of cell lysates from stable RPE1 cells under serum starvation conditions (24 h) in absence (-) and presence (+) of DOX (1 µg/ml, 24 h) and/or epidermal growth factor (EGF) (100 ng/ml, 10 min). Whole cell lysates were analyzed using the indicated antibodies. (**D**) Normalized cellular ATP content from HCT 116 and RPE1 cells transduced with RBDwt (blue), RBDv1 (magenta) or RBDv12 (orange) measured by luciferase mediated bioluminescence. Reduction of cellular ATP in presence of RBDs (+DOX) was monitored after 120 h induction and normalized to the luminescence of non-induced control (-DOX) cells. (**E**) Quantification of flow cytometry data of annexin V antibody and propidium iodide (PI) stained HCT 116 and RPE1 cells cultured under full medium conditions in absence (-DOX) or presence (+DOX) (1 µg/ml, 72 h). (**F**)

Quantification of flow cytometry data as in (E) of RPE1 cells cultured under serum starvation conditions in absence (-DOX) or presence (+DOX) (1 µg/ml, 24 h). Error bars corresponds to ± standard deviation (SD) of 3 biological replicates (n=3). P-values were calculated by an unpaired t test ($^{*}P$< 0.05, *P< 0.01, $^{***}P$< 0.005).

Figure 5

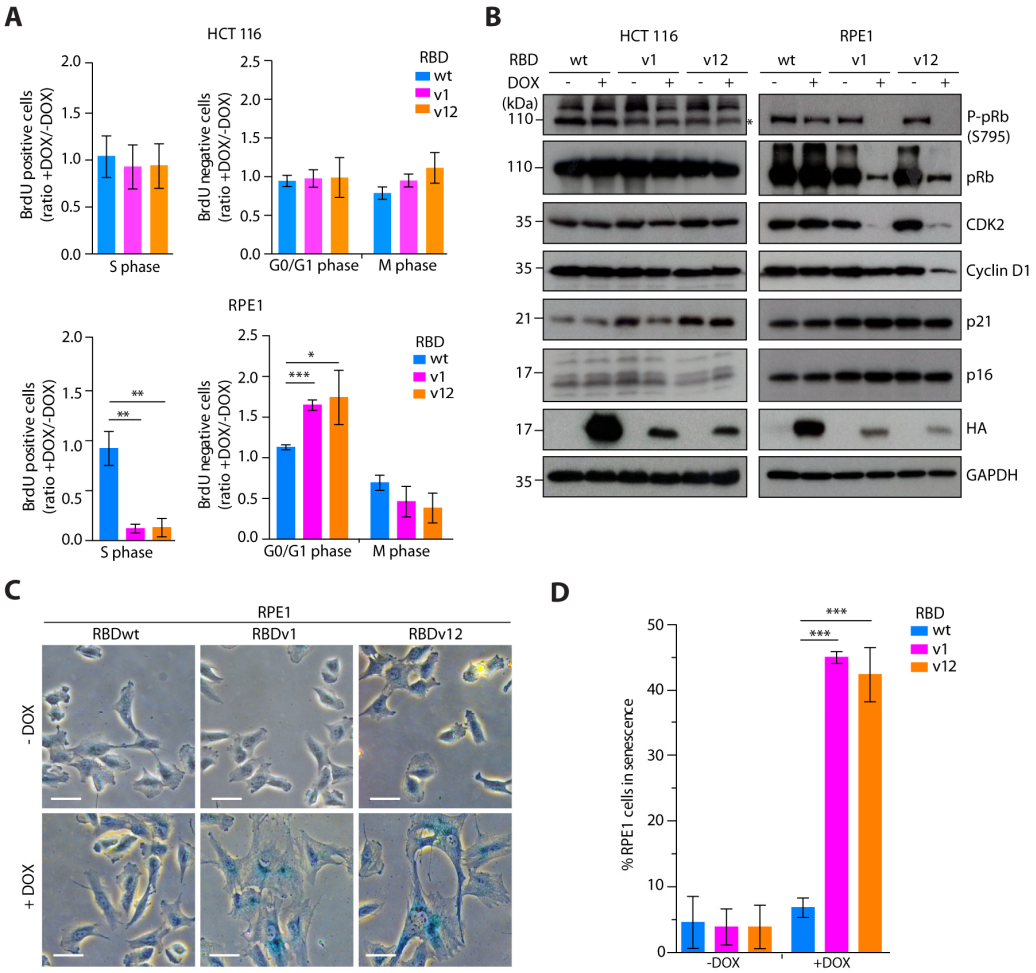

Fig. 5. RPE1 cells show cell cycle arrest, absent phosphorylation of retinoblastoma protein (pRb) and become senescent within 24 h in the presence of inhibitory RBDvs. (**A**) HCT 116 and RPE1 cells stably transduced with doxycycline inducible lentiviral constructs expressing RBDwt (blue), RBDv1 (magenta) or RBDv12 (orange) were assayed by flow cytometry for incorporation of 5-bromo-2'-deoxyuridine (BrdU) and propidium iodide (PI). Data shows ratios of cell population corresponding to S-, G0/G1- and M-phase upon doxycycline induction (+DOX) (1 µg/ml, 72h) relative to non-induced controls (-DOX). Error bars correspond to ± SD of three independent replicates (n=3). P-values were calculated by an unpaired t test ($^{*}P< 0.05$, $^{**}P< 0.01$ and $^{***}P< 0.005$). (**B**) Immunoblot analysis of stable HCT 116 and RPE1 cells used in expressing HA-tagged RBDwt or RBDvs upon DOX induction (1 µg/ml, 24 h). Whole cell lysates were analyzed using the indicated antibodies. Asterisk indicates specific band. (**C**) Bright field microscopy images of stable RPE1 cells expressing HA-tagged RBDwt or RBDvs upon DOX induction (1 µg/ml, 24 h) stained for senescence-

associated β-galactosidase (SA-β-Gal) activity. Scale bars: 50 µm. (**D**) Quantification of flow cytometry data of stable RPE1 cells expressing HA-tagged RBDwt (blue), RBDv1 (magenta) or RBDv12 (orange) upon DOX induction (1 µg/ml, 48 h) stained for SA-β-Gal activity. Data are mean ± SD of three biological replicates. P-values were calculated as before.

Figure 6

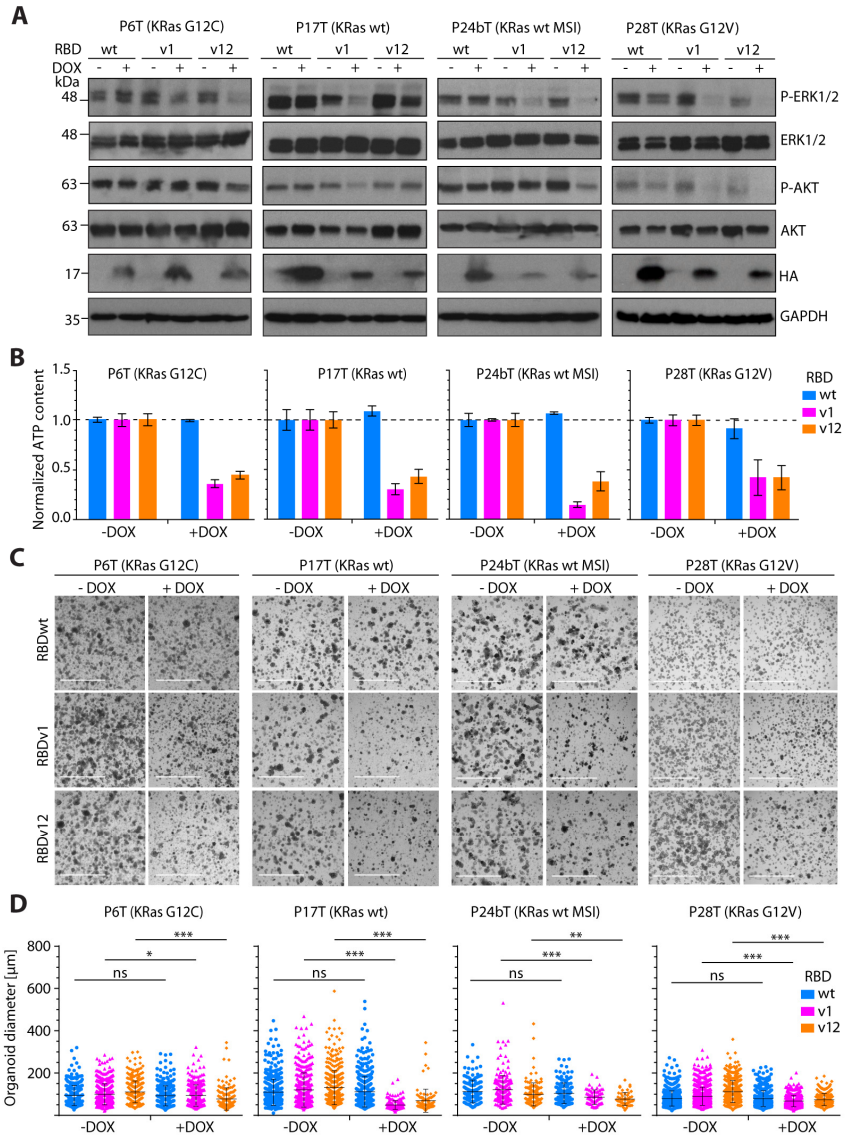

Fig. 6. Patient-derived colorectal cancer (CRC) organoids show reduced MAPK and AKT signaling and reduced cell viability upon RBDvs expression. (**A**) Immunoblot of whole cell lysates derived from indicated patient-derived CRC organoids stably transduced with lentivirus encoding HA-tagged RBDwt, RBDv1 and RBDv12 in absence (-) or presence (+) of DOX (2 µg/ml, 72 h). Cell lysates were analyzed using indicated antibodies. (**B**) Cellular ATP content of organoid cultures used in (A) expressing RBDwt (blue), RBDv1 (magenta) and RBDv12 (orange) was measured in a luciferase mediated bioluminescence assay. Reduction of cellular ATP in presence of RBDvs (+DOX) in P17T and P24bT was monitored after 72 h induction and normalized to the luminescence of non-induced control organoids (-DOX) (2 µg/ml, 72 h). P6T and P28T stable organoids were seeded as single cells and induced for 96 h and analyzed as above. Error bars correspond to ± SD of three technical replicates (n=3). (**C**)

Bright field microscope images of organoid cultures used in (A) in presence (+) or absence (-) of DOX (2 µg/ml, 72 h). Scale bars correspond to 2 mm. P=patient; T=tumor, MSI=microsatellite instability. (**D**) Quantification of organoid size in presence and absence of DOX (2 µg/ml, 2-6 d) from bright field microscope images of organoid lines used in (A). Error bars correspond to ± SD. Statistics were calculated using the Mann-Whitney U-test ($^{*}P < 0.05$, $^{**}P < 0.01$ and $^{***}P < 0.005$).

Supplementary Text:

Methods

Ras expression, purification and nucleotide exchange

The human HRas (AA 1-166) and KRas (AA 1-169, isoform B) proteins were expressed as GST-fusions from pGEX-6P-1 plasmids for selection experiments and as His-tag fusions from pET-53 plasmids for *in vitro* competition and binding assays. Plasmids were used to transform *E. coli* Rosetta(DE3) cells and individual colonies were handled essentially as written before [15], except that all buffers were supplemented with 5 mM $MgCl_2$. Briefly, resulting cultures from individual colonies were inoculated into Luria Broth (LB) media and protein expression was induced at OD_{600}=0.8 with 0.5 mM IPTG. After overnight incubation at 16 °C, bacterial pellets were resuspended in 50 mM Tris-HCl pH 7.5, 150 mM NaCl, 1 mM PMSF and 5 mM $MgCl_2$ and lysed by sonication. The lysates were clarified by centrifugation and proteins in the supernatant were purified using Ni-NTA chromatography (Qiagen) for His-tagged proteins or Glutathione Sepharose 4 Fast Flow beads (GE Healthcare) for GST-tagged proteins at 4 °C following the manufacturer's instructions. Eluted fractions were dialyzed into 150 mM NaCl, 50 mM Tris-HCl pH 7.5, 1 mM DTT and 5 mM $MgCl_2$ and protein concentrations were determined by measuring the absorption at 280 nm.

Nucleotide exchange to GTPγS or GDP was performed by the addition of 10-fold molar excess of GTPγS or GDP (Sigma Aldrich) and 5 mM EDTA to dialyzed proteins. After 30 min incubation at 37 °C, proteins were transferred on ice and exchange was quenched by the addition of 10 mM $MgCl_2$ final concentration.

Construction of a phage-displayed CRAF-RBD library

For phage library construction, Ras-binding domain (RBD) of human CRAF kinase (AA 55-131) was cloned into the phagemid pNE [14] and cysteines at position 81, 95 and 96 of the RBD were mutated to serines using site-directed mutagenesis [32]. Afterwards, two degenerate oligonucleotides were used to introduce mutations at 2 regions of the RBD gene by site-directed mutagenesis. Oligonucleotides were soft-randomized as described before [14, 15]. The nucleotide ratio was adjusted to 70 % of the wt nucleotide represented N1 = A, N2 = C, N3 = G and N4 = T and 10 % of each of the other three nucleotides.

Oligonucleotide 1: GAT GAC AAA AGC AAC N1N2N4 ATC N2N3N4 GTT N4N4N2 TTG CCG AAC N1N1N3 N2N1N1 N1N3N1 ACA N3N4N3 GTC N1N1N4 GTG CGA AAT GGA ATG

Oligonucleotide 2: CAT GAC TGC CTT ATG N1N1N1 N3N2N1 CTC N1N1N3 N3N4N3 N2N3N3 N3N3N2 CTG CAG CCA GAG TGC

The resulting library was used to electroporate *E. coli* SS320 cells using established methods resulting in $2.2x10^9$ independent RBD variants [33].

RBD variant selection against activated HRas

Library pool of phage displaying individual RBD variants were harvested by precipitation with PEG/NaCl (20 % PEG-8000 (w/v), 2.5 M NaCl) and resuspended in PBT buffer (1x PBS, 1 % BSA, 0.1 % Tween 20) supplemented with 5 mM $MgCl_2$. Immobilization of GTPγS-loaded GST-tagged HRas and subsequent binding selections were done essentially as described before [15], except that all buffers were supplemented with 5 mM $MgCl_2$. In brief, 4 wells of a 96 well Maxisorp microtiter plate (NUNC) were coated with 100 µl of 2 µM GST-tagged GTPγS-loaded HRas in dialysis buffer (150 mM NaCl, 50 mM Tris-HCl pH 7.5, 1 mM DTT and 5 mM $MgCl_2$) over night at 4 °C. After blocking with PBT buffer for 1 h, phage library pool was added to each well and incubated for 1 hour at 4 °C. The plate was washed 8 times with cold PT buffer (1x PBS, 0.1 % Tween 20) and bound phage were eluted with 0.1 M HCl and immediately neutralized with 1.0 M Tris-HCl pH 8.0. Eluted phage were directly used to infect exponentially growing *E. coli* XL1-blue supplemented with helper phage M13K07 (NEB) and incubated over night at 37 °C. In each successive selection round, the selection stringency was increased by 2 additional washing steps and. To avoid unspecific binding towards the GST-tag, a GST counter-selection was performed starting with round 2. Additionally, after 3 rounds of selection, phage binding and washing was done at room temperature and the concentration of coated GST-tagged GTPγS-loaded HRas was reduced to 0.5 µM. After five rounds of enrichment, individual RBD variants with improved binding properties towards active HRas were identified by clonal phage ELISA as described [33]. In brief, phage displaying individual RBD variants were prepared from single colonies of bacteria harboring phagemids encoding RBDvs and transferred to 384-well Maxisorp plates immobilized with GST-tagged GTPγS-labelled HRas (0.5 µM) and blocked with BSA, as described previously. As negative controls, wells were coated with GST or only blocked with BSA. After incubation, washing and developing, positive clones were further analysed by sequencing.

Cloning of RBD variants

DNA fragments encoding the selected variants and the unmodified RBDwt were cloned into pDONR233 plasmids by Gateway cloning (Invitrogen) as described before [15]. Further recombination into the Gateway destination vectors pET53DEST, pDEST15 and pLDT-NT-HA was performed according to the manufacturer's instructions (Invitrogen).

RBDvs protein expression and purification

For competitive *in vitro* pull-down experiments and bio-layer interferometry measurements, His-tagged (from pET53DEST plasmids) and GST-tagged (from pGEX-6p-1 plasmids) RBD variants and RBDwt, Ras-association domain (RA) of RalGDS (AA 798-885) and GST alone were processed as Ras proteins (see above).

Competitive *in vitro* pull-down experiment

The Ras/RBDwt competition assay was performed in 200 µl assay buffer (25 mM Tris-HCl pH 7.5, 150 mM NaCl, 1 % NP-40, 5 mM $MgCl_2$ and 5 % glycerol) using 8 µg (1.15 µM) GST-tagged RBDwt or RalGDS-RA bound to GSH-sepharose beads. First, 5 µg (1.15 µM) of His-tagged KRas loaded with GTPγS was incubated with His-tagged RBDwt or RBDvs with increasing concentrations (2.3 µg [1.15 µM], 5.8 µg [2.68 µM] and 23 µg [11.5 µM], which corresponds to a molar ratio of 1:1, 1:2.5 and 1:10 of GST-tagged RBDwt or RalGDS-RA:His-tagged RBDwt or RBDvs) for 30 min at 4 °C with end-over-end rotation. 8 µg of beads were added to the reaction mix and incubated for another 30 min at 4 °C. After 2 washes with assay buffer, beads were resuspended in 30 µl 2x SDS sample buffer and incubated for 5 min at 95 °C. Controls samples consisted of GTPγS- or GDP-loaded KRas incubated with GST-RBDwt or GST-RalGDS-RA beads. Also, GTPγS-loaded KRas was incubated with GST bound to beads. Samples were analyzed by immunoblot using anti-Ras antibody (#16117 ThermoFischer Scientific) and membrane was stained with Ponceau S as loading control.

Bio-layer interferometry (BLI)

Kinetic binding assays were performed on Octet RED96 instrument (Pall ForteBio). Dialyzed proteins were supplemented with 0.1 % BSA and 0.02 % Tween 20. GST or GST-tagged RBDvs were immobilized onto anti-GST biosensors (Pall ForteBio) at a concentration of 2 µg/ml.

Association was analyzed at concentrations starting from 1000 nM to 15.6 nM in 1:1 dilution steps of GTPγS- or GDP-loaded HRas. Dissociation was measured in dialysis buffer (150 mM NaCl, 50 mM Tris-HCl pH 7.5, 1 mM DTT and 5 mM $MgCl_2$) supplemented with 0.1 % BSA and 0.02 % Tween 20. Non-specific interaction of HRas with biosensors was assayed using empty anti-GST sensors. Reference wells were subtracted from sample wells and a 1:1 global fitting model was used to determine k_{on}, k_{off} and K_d values.

Protein expression and purification for crystallography

RBDv1, RBDv12 and HRas G12V (residues 1-166) were expressed as TEV protease cleavable GST-fusions using a modified pGEX-2T vector. Expression constructs were transformed into BL21-CodonPlus DE3-RIL bacteria (Agilent Technologies) for protein production. Bacterial expression was induced overnight at 18 °C with 0.5 mM IPTG and was performed in LB media. RBDvs bacterial pellets were resuspended in 50 mM HEPES pH 7.5, 300 mM NaCl, 5 % glycerol, 1 mM PMSF, 1 mM TCEP and lysed by homogenization. The lysate was cleared by centrifugation at 4 °C for 40 minutes at 18,000 g. Protein was bound to glutathione affinity resin (GE Healthcare), eluted by cleavage of the GST-tag with TEV, concentrated and then buffer exchanged by size exclusion chromatography (SEC) using a Superdex75 24 ml column (GE healthcare) equilibrated in 50 mM HEPES pH 7.5, 50 mM NaCl, 5 % glycerol, 10 mM $MgCl_2$, 1 mM TCEP.

HRas G12V bacterial pellets were resuspended in 50 mM HEPES pH7.5, 300 mM NaCl, 5 mM EDTA, 5 % glycerol, 1 mM PMSF, 1 mM TCEP and lysed by homogenization. The lysate was clarified by centrifugation at 4 °C for 40 minutes at 18,000 g. Protein was bound to glutathione affinity resin (GE Healthcare), washed with 50 mM HEPES pH 7.5, 300 mM NaCl, 25 mM imidazole, 5 % glycerol, 1 mM TCEP and eluted by cleavage of the GST-tag with TEV, concentrated and then buffer exchanged by SEC using a Superdex75 24 ml column equilibrated in 50 mM HEPES pH7.5, 300 mM NaCl, 5 mM EDTA, 5 % glycerol, 1 mM TCEP. GMP-PNP loading on HRas G12V was carried out by incubating purified HRas G12V with 10-fold excess of GMP-PNP for 80 min at 4 ˚C followed by the addition of 30-fold excess of $MgCl_2$ for 120 min at 4 ˚C.

The RBDvs:HRas G12V complexes were obtained by mixing RBDvs and GMP-PNP loaded HRas G12V at equal molar ratio for 60 min at 4 ˚C followed by SEC using a Superdex75 24 ml column equilibrated in 50 mM HEPES pH 7.5, 50 mM NaCl, 10 mM $MgCl_2$, 5 % glycerol, 1 mM TCEP. All

fractions corresponding to co-elution of HRas G12V with RBDvs were pooled and concentrated to 12.2 mg/ml, then flash frozen in liquid nitrogen. Protein concentration was estimated by UV-Vis absorption spectroscopy using a NanoDrop spectrophotometer (Thermo-Fisher Scientific).

Protein crystallography, data collection and structural analysis.

The RBDvs:HRas G12V complexes were crystallized at 20 ˚C in sitting-drop by mixing 0.5 µL of complexes (450 µM, 12.2 mg/ml) with 0.5 µL of mother liquor of 0.1 M sodium cacodylate pH 6.5, 200 mM ammonium sulphate, 30 % PEG 4000 or mother liquor of 0.1 M sodium citrate pH 5.6, 200 mM ammonium sulphate, 30 % PEG 4000 for RBDv1:HRas G12V and RBDv12:HRas G12V, respectively. X-ray diffraction data were collected on a flash-frozen crystal cryo-protected in mother liquor containing 25 % glycerol at 100 K on station 24-ID-C, NE CAT beamline, Advanced Photon Source (APS). Data reduction was performed using XDS package [34]. The structure was solved by molecular replacement using PDB 4G0N [20] as a search model in Phaser [35]. Model building and refinement was performed using COOT [36], LORESTR [37] and REFMAC [38] from the CCP4 suite [39]. The data statistics and refinement details are reported in Supplementary Table 1.

Cell culture

HCT 116 (#CCL-247) and hTERT RPE1 (#CRL-4000) cells were purchased from ATCC and handled according to the supplier's instructions. MIA PaCa-2, A549 and H1299 cell lines were cultured in DMEM (MIA PaCa-2 and A549) or RPMI-1640 (H1299) medium (both Gibco) supplemented with 10% (v/v) fetal bovine serum (Gibco). Cell lines were tested and found to be mycoplasma-free. Stable cell lines were constructed using lentiviral vectors (pLDT) encoding N-terminally HA-tagged RBDvs and wt under the control of a doxycycline inducible promotor by standard techniques [40]. The original pLDT plasmid was a gift from Jason Moffat (University of Toronto, The Donnelly Centre, 160 College St., Toronto). Two days after transduction, cell lines were selected with 2 µg/ml puromycin for HCT 116, MIA PaCa-2, A549 and H1299 and 10 µg/ml puromycin for and RPE1. For all experiments, 1 µg/ml doxycycline was used to induce expression of HA-tagged RBDvs or RBDwt.

Immunoprecipitation for mass spectrometry

Two 10 cm dishes per construct (RBDwt, v1 and v12) were seeded with $2x10^6$/ml stable HCT 116 cells and RBDvs expression was induced 24 h later with doxycycline. After 24 h induction, cells were scraped into 1x PBS and washed twice with 1x PBS. After centrifugation, the cell pellets were resuspended in lysis buffer (25 mM Tris-HCl pH 7.5, 150 mM NaCl, 1 % NP-40, 5 mM $MgCl_2$, 5 % glycerol and protease inhibitor cocktail [Roche]) and incubated for 20 min at 4 °C with end-over-end rotation. The lysates were centrifuged, supernatants were transferred to 20 µl pre-equilibrated anti-HA affinity matrix (Roche) and incubated for 40 min at 4 °C. Beads were washed 2 times with 500 µl lysis buffer. Elution was performed by the addition of 20 µl 2x SDS-sample buffer to the beads and incubation for 3 min at 95 °C. 5 µl of samples were analysed by immunoblotting using antibodies against endogenous Ras, HA-tag and GAPDH (#3965, #2999 and #8884, respectively; all from Cell Signaling Technology). Sample preparation for in-gel digest was done as described before [41]. In brief, supernatants were loaded onto SDS-polyacrylamide gel and the gel was stained using InstantBlue (Expedeon). Gel lanes were cut into pieces and subsequently washed, destained and dehydrated. Proteins were reduced with 10 mM dithiothreitol (DTT), alkylated with 55 mM iodoacetamide (IAA) and digested overnight with sequencing-grade Trypsin (Promega). Peptides were extracted using an increasing concentration of acetonitrile. Finally, peptides were concentrated and desalted using the Stop and Go Extraction (STAGE) technique [42].

Liquid chromatography and mass spectrometry

A binary buffer system consisting of buffer A (0.1 % formic acid) and buffer B (80 % acetonitrile, 0.1 % formic acid) was used for peptide separation on an Easy-nLC 1200 (Thermo Fisher Scientific). This system was coupled *via* a nano electrospray ionization source to the quadrupole-based Q Exactive HF benchtop mass spectrometer [43]. Peptide elution from the in-house packed 18 cm (1.9 µm C18 Beads, Dr. Maisch, Germany) column was achieved by increasing the relative amount of B from 10 % to 38 % in a linear gradient within 23 min at a column temperature of 40 °C. Followed by an increase to 100 % B within 7 min, gradients were completed by a re-equilibration to 5 % B.

Q Exactive HF settings: MS spectra were acquired using 3E6 as an AGC target, a maximal injection time of 20 ms and a 60,000 resolution at 300 m/z. The mass spectrometer operated in a data dependent Top15 mode with subsequent acquisition of higher-energy collisional dissociation (HCD) fragmentation MS/MS spectra of the top 15 most intense peaks. Resolution

for MS/MS spectra was set to 30,000 at 200 m/z, AGC target to 1E5, maximal injection time to 64 ms and the isolation window to 1.6 Th.

Mass spectrometry data processing and analysis

All acquired raw files were processed using MaxQuant (1.5.3.30) [44] and the implemented Andromeda search engine [45]. For protein assignment, electrospray ionization-tandem mass spectrometry (ESI-MS/MS) fragmentation spectra were correlated with the Uniprot human database (v. 2016) including 4 manually added sequences of the RBD variants and KRas G13D (RBDwt: MGYPYDVPDYAGQGPDPSTNSADITSLYK KAGFSNTIRVFLPNKQRTVVNVRNGMSLHDCLMKALKVRGLQPECCAVFRLLHEHKGKKARLDWNTDA ASLIGEELQVDFL; RBDv1: MGYPYDVPDYAGQGPDPSTNSADIT SLYKKAGFSNTIRVLLPNQEWTVVKVRNGMSLHDSLMKALKRHGLQPESSAVFRLLHEHKGKKARLDW NTDAASLIGEELQVDFL; RBDv12: MGYPYDVPDYAGQGPDPST NSADITSLYKKAGFSNTIRVLLPNHERTVVKVRNGMSLHDSLMKALKRHGLQPESSAVFRLLHEHKGKKA RLDWNTDAASLIGEELQVDFL; KRas G13D: MTEYKLVVVGAGD VGKSALTIQLIQNHFVDEYDPTIEDSYRKQVVIDGETCLLDILDTAGQEEYSAMRDQYMRTGEGFLCVFAI NNTKSFEDIHHYREQIKRVKDSEDVPMVLVGNKCDLPSRTVDTKQAQDLARSYGIPFIETSAKTRQGVDD AFYTLVREIRKHKEKMSKDGKKKKKKSKTKCVIM). Searches were performed with tryptic specifications and default settings for mass tolerances for MS and MS/MS spectra. Carbamidomethyl at cysteine residues was set as a fixed modification, while oxidation at methionine and acetylation at the N-terminus were defined as variable modifications. The minimal peptide length was set to seven amino acids and the false discovery rate for proteins and peptide-spectrum matches to 1 %. The match-between-run feature was used with a time window of 0.7 min. Relative label-free quantification of proteins was done using the MaxLFQ algorithm integrated into MaxQuant [46]. The minimum LFQ ratio count was set to 2 and the FastLFQ option was enabled.

For subsequent analysis, the Perseus software (1.5.3.0) [47] was used and first filtered for contaminants and reverse entries and proteins that were only identified by site. The LFQ intensities were logarithmized to base 2 and grouped into duplicates. To overcome the missing value problem in immunoprecipitation data, proteins that were quantified less than 2 times in one of the experimental groups were discarded from further analysis. Missing values were

imputed column-wise by a down-shifted (median-1.8) Gaussian distribution mimicking the detection limit of the mass spectrometer.

Metabolic activity assay

1000 cells of each stable cell line were seeded in a 96 well plate in duplicates. The following day, expression was induced by the addition of doxycycline. Corresponding control wells were not induced. Cell viability was assayed 120 h after induction using CellTiter-Glo (Promega). Luminescence signals of induced wells were normalized to uninduced well data.

Immunoblotting

Stable cell lines were seeded in 6 well plates (1×10^5 cells/well) and induced 24 h later with doxycycline (1µg/ml). Control cells were left uninduced. 24 h after induction, cells were washed twice with 1x PBS and lysed in 200 µl 2x SDS sample buffer. Whole cell lysates were analyzed by immunoblot using the indicated antibodies. For serum starvation experiments, medium was replaced upon induction with serum-free medium. 24 h after induction, cells were treated with 100 ng/ml EGF (Sigma) for 10 min before lysis.

Antibodies

Antibodies used for western blot analysis were: phospho-MEK1/2 (Ser217/221) (clone 41G9 #9154), MEK1/2 (clone D1A5 #8727), pospho-ERK1/2 (p44/42 MAPK) (Thr202/Tyr204) (clone D13.14.4E #4370), ERK1/2 (p44/42 MAPK) (clone 137F5 #4695), phospho-AKT (Ser473) (clone D9E #4060), AKT (clone C67E7 #4691), phospho-pRb (Ser795) (#9301), GAPDH-HRP (clone D16H11 #8884), HA-HRP (clone 6E2 #2999) and cyclin D1 (clone 92G2 #2978) were purchased from Cell Signaling Technologies. Other antibodies used: pRb (clone EPR17512 #181616, Abcam), CDK2 (clone M2 #sc163, Santa Cruz), p21 (clone C-19 #sc397, Santa Cruz), CDKN2A/p16INK4a (clone 2D9A12 #ab54210, Abcam).

Analysis of cell growth by real-time cell analysis (RTCA)

Cell proliferation of stably transduced HCT 116 and RPE1 cells was assessed using xCELLigence real-time cell analysis (RTCA) SP (single plate) system (ACEA Biosciences). 1000 cells/well were seeded in a 96-well electronic microtiter plate (ACEA Biosciences) with 200 µl medium/well.

After 24 h, cells were induced by doxycycline. Cell proliferation was monitored for 120 h. Experiments were performed as duplicates and repeated at least twice.

Apoptosis and cell cycle analysis by flow cytometry

Stably transduced HCT 116 or RPE1 cells were seeded in 6-well plates (1×10^5 cells/well) and induced 24 h later with doxycycline. Control cells were left uninduced. After 72 h, cells were washed once with 1x PBS. For analysis of apoptotic cells, Annexin V-FITC apoptosis detection kit (#ALX-850-020 Enzo) was used following the manufacturer's protocol. For analysis of serum-starved RPE1 cells, 2×10^5 cells/well of stably transduced PRE1 cells were seeded in 6-well plates. 24 h later, cells were washed twice with 1x PBS and serum-free medium and doxycycline were added to the wells. After 24h, cells were washed once with 1x PBS and analysed with Annexin V-FITC apoptosis detection kit.

Cell cycle analysis was performed as described before [48]. In short, cells were treated with bromodeoxyuridine (BrdU) (20 µM, #B5002 Sigma-Aldrich) for 4 h, washed with 1x PBS and trypsinized. Afterwards, cells were fixed in 70 % ethanol and BrdU incorporation was measured by staining with anti-BrdU antibody (#555627 BD Biosciences) and Alexa Fluor 488-conjugated antibody (#A21202 Thermo Fischer Scientific) along with propidium iodide (PI) to stain DNA content.

All samples were analyzed on a FACSCanto II flow cytometer (BD Biosciences) and data were processed by FlowJo software (FlowJo, LLC). Gating was done based on viable and single cells that were identified on the basis of scatter morphology.

Senescence analysis by light microscopy

Cellular senescence was performed using Senescence β-Galactosidase Staining Kit (#9860 Cell Signaling Technologies) following the manufacturer's protocol. Senescence was analyzed under a bright field microscope (Leica DM IL LED). For wash out experiments, cells were induced for 24 h, washed twice with 1x PBS and left for another 24 or 48 h in full medium before staining.

Senescence analysis by flow cytometry

Flow cytometry analysis of senescent cells was performed using the Cellular senescence live cell analysis assay (#130-0010 Enzo) following the manufacturer's protocol. Samples were

analyzed on a FACSCanto II flow cytometer (BD Biosciences), and data were processed by FlowJo software (FlowJo, LLC). Gating was done based on viable cells that were identified on the basis of scatter morphology.

Organoid cultures

Human tumor colon organoid samples were obtained from a published colorectal cancer organoid biobank [27]. Resection tissues were obtained with written informed consent, and following approval by the ethics committees of the Diakonessen Hospital, Utrecht. Tissue was obtained with written informed consent and following approval, according to the guidelines of the University Cancer Center (UCT), Frankfurt. Organoid cultures were established and maintained as described previously [49]. Tumor organoids were maintained in medium lacking Wnt3a. The organoid lines were transduced as described [50] with lentivirus expressing N-terminally HA-tagged RBDwt, RBDv1 or RBDv12 (as above). Three days after transduction, organoids were selected with 1 µg/mL puromycin in the culture medium. For cell viability assays, the cells were seeded in Matrigel either following mechanical dissociation or enzymatic single cell dispersal using TrypLE Express reagent (Gibco). 2 µg/mL doxycycline was added 1 day after seeding. After 3 days cell viability was measured using CellTiter-Glo reagent (Promega). All experiments were measured as technical triplicates and the experiments were repeated at least twice each.

For quantification of organoid size, light microscopy pictures were taken at a 2x resolution after 2-6 days of doxycycline exposure, as indicated. The diameter (µm) of all viable organoids in one picture of each condition was measured using ImageJ. Viable organoids were identified as refringent, while dark structures surrounded by cell debris were excluded from the analysis. The quantification was performed on two independent experiments.

Statistical methods

Data are presented as the mean ± standard deviation (SD). The comparisons between RBDwt and RBDvs were made by an unpaired t test using GraphPad Prism software. For statistical analysis of the quantification results of organoid sizes, a Mann-Whitney U-test was performed using GraphPad Prism software. The level of significance was set at $^{*}P < 0.05$, $^{**}P < 0.01$ and $^{***}P < 0.005$.

Supplementary Figures and Tables:

Supplementary Fig. 1

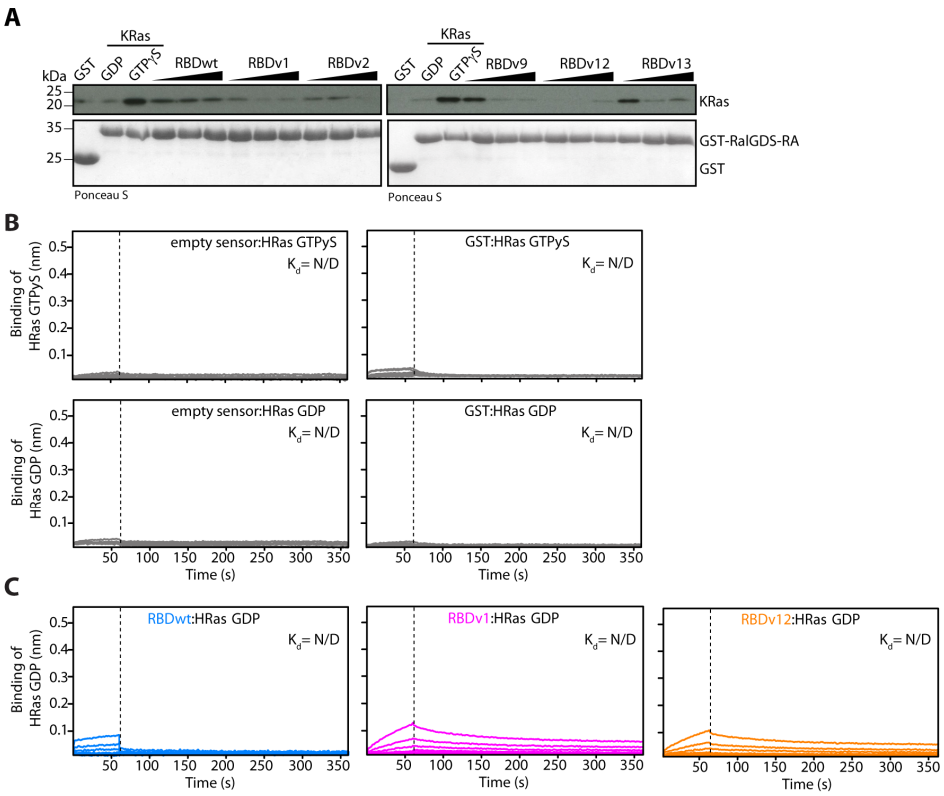

Supplementary Fig. 1. RBDvs outcompete RalGDS-Ras association domain (RA) binding to activated KRas and do not bind to inactive HRas. (**A**) *In vitro* competition of increasing concentration of His-tagged RBDvs and RBDwt and GST-tagged RalGDS-RA immobilized on glutathione sepharose beads binding to His-tagged GTPγS-loaded KRas. KRas bound to beads was detected by immunoblot and the corresponding Ponceau S stained membrane is shown. (**B**) Control experiments of GDP- or GTPγS-loaded HRas and immobilized GST or empty anti-GST biosensors measured by bio-layer interferometry. Concentrations of Ras ranged from 1 µM to 15.6 nM in a 1:1 dilution series. (**C**) Binding of GDP-loaded HRas to immobilized GST-tagged RBDwt (blue), RBDv1 (magenta) or RBDv12 (orange) measured by bio-layer interferometry. Concentrations of Ras were as described in (B). K_d values for could not be calculated due to weak binding. N/D.=not determined.

Supplemental Fig. 2

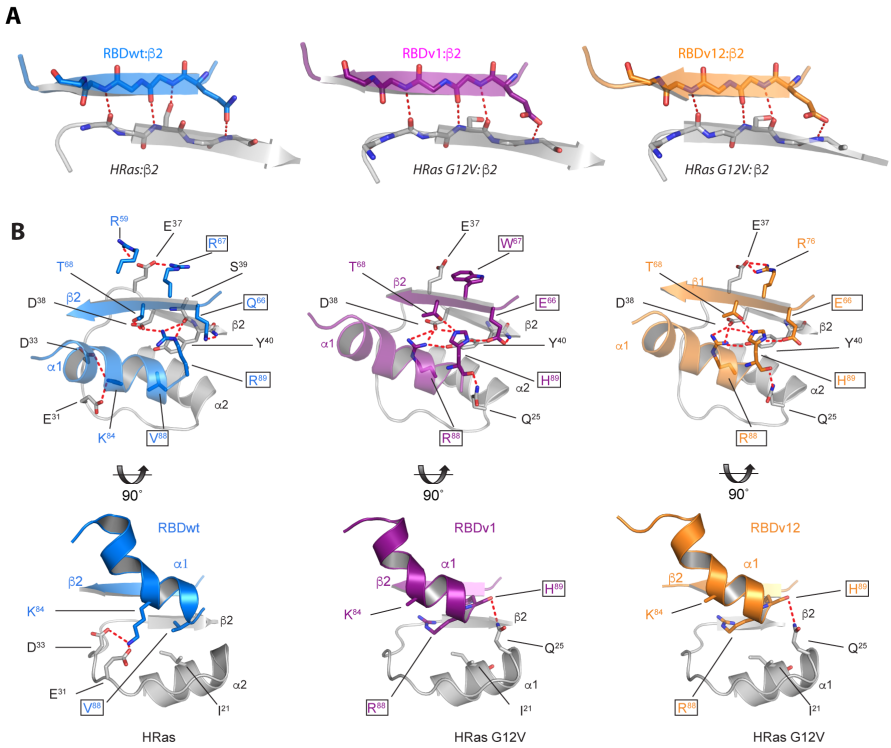

Supplementary Fig. 2. RBDvs bind to HRas through a canonical binding mode. (**A**) Detailed view of the canonical extended intermolecular β-sheet at the binding interface of the RBDwt or RBDvs with HRas or HRas G12V, respectively. Coloring and labeling are as in Fig. 1E. (**B**) Top and side view of the binding interface of RBDwt and RBDvs with HRas. Residues involved in intermolecular interactions are shown as stick. Residues that are mutated in RBDvs are highlighted by a black square. 90° rotated side view highlights the steric clash between Ile^{21} in HRas and Val^{88} to Arg in RBDvs that is involved in a shift of the α1-helix of the RBDvs relative to that observed in RBDwt.

Supplementary Fig. 3

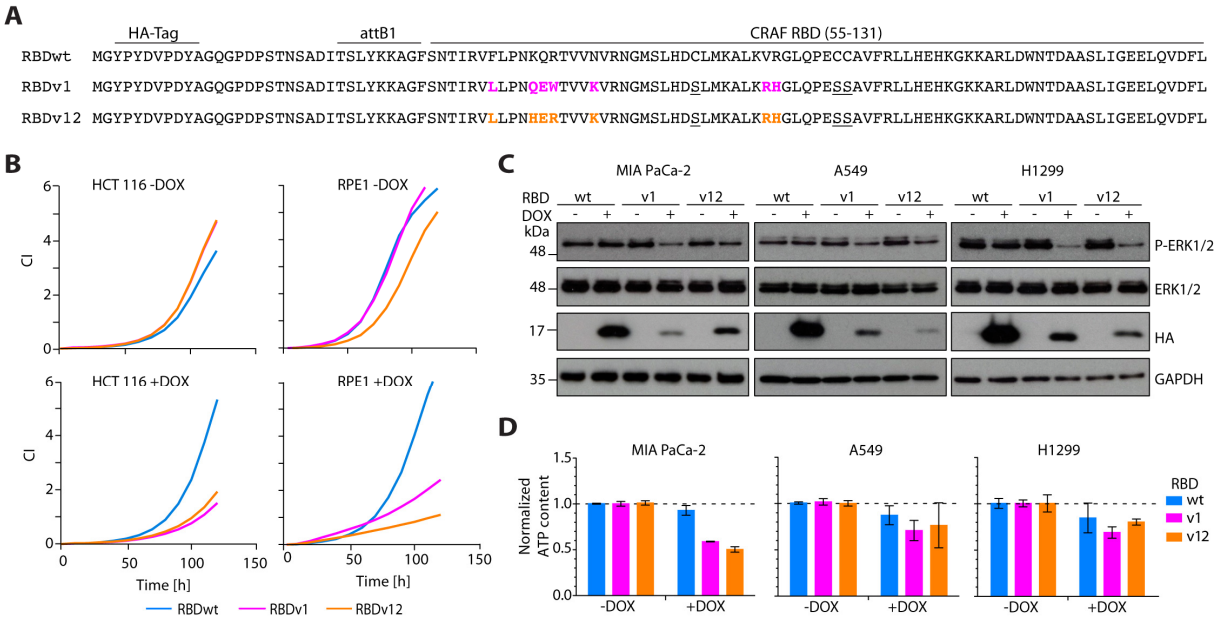

Supplementary Fig. 3. RBDvs lead to reduced cell proliferation in HCT 116 and RPE1 cells and reduce MAPK signaling in various cancer cell lines. (**A**) Amino acid sequences of HA-tagged RBDwt or RBDvs that were used in this study. Highlighted in bold (magenta and orange in RBDv1 and RBDv12, respectively) are those amino acids that differ from the RBDwt sequence. Underlined are the cysteine to serine mutations in RBDv1 and v12. (**B**) Cellular growth measured following cell index (CI) over time (h) by Real-time cell analysis (RTCA) of HCT 116 and RPE1 cells in absence or presence of DOX (1 µg/ml, 120 h). The mean of two technical replicates is shown. (**C**) Immunoblot of whole cell lysates derived from indicated cell lines stably transduced with lentivirus encoding HA-tagged RBDwt, RBDv1 and RBDv12 in absence (-) or presence (+) of DOX (1 µg/ml, 24 h). Cell lysates were analyzed using indicated antibodies. (**D**) Cellular ATP content of cell lines used in (B) expressing RBDwt (blue), RBDv1 (magenta) and RBDv12 (orange) was measured in a luciferase mediated bioluminescence assay. Reduction of cellular ATP in presence of RBDvs (+DOX) was monitored after 120 h induction and normalized to the luminescence of non-induced control organoids (-DOX) (1 µg/ml, 120 h). Error bars correspond to ± SD of three technical replicates (n=3).

Supplementary Fig. 4

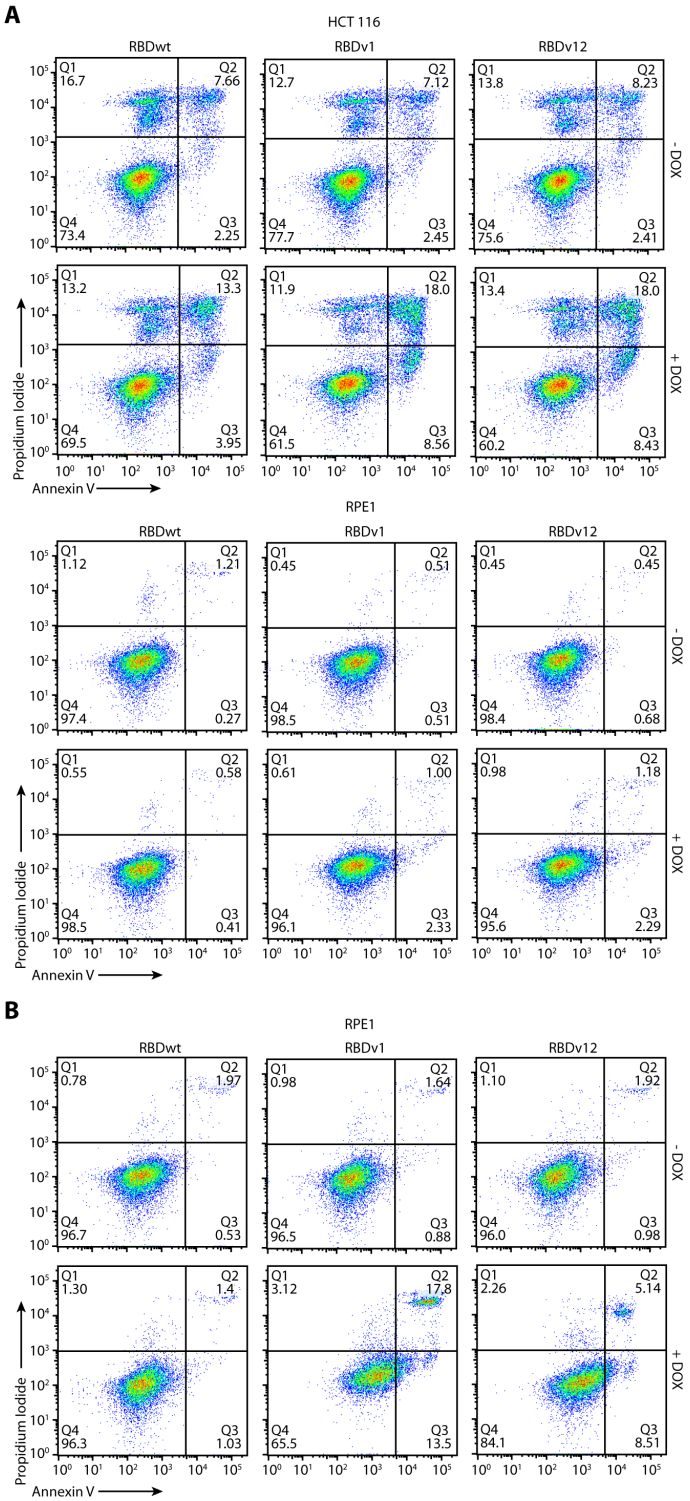

Supplementary Fig. 4. RBDvs induce apoptosis in stable HCT 116 and in serum-starved RPE1 cells. Representative flow cytometry analysis of HCT 116 and/or RPE1 cells stained with fluorophore labeled annexin V antibody and propidium iodide (PI) by flow cytometry in absence (-DOX) or presence (+DOX) of DOX (**A**) under full medium conditions (DOX 1 µg/ml, 72 h) and (**B**) under serum-starved conditions (DOX 1 µg/ml, 24 h).

Supplementary Fig. 5

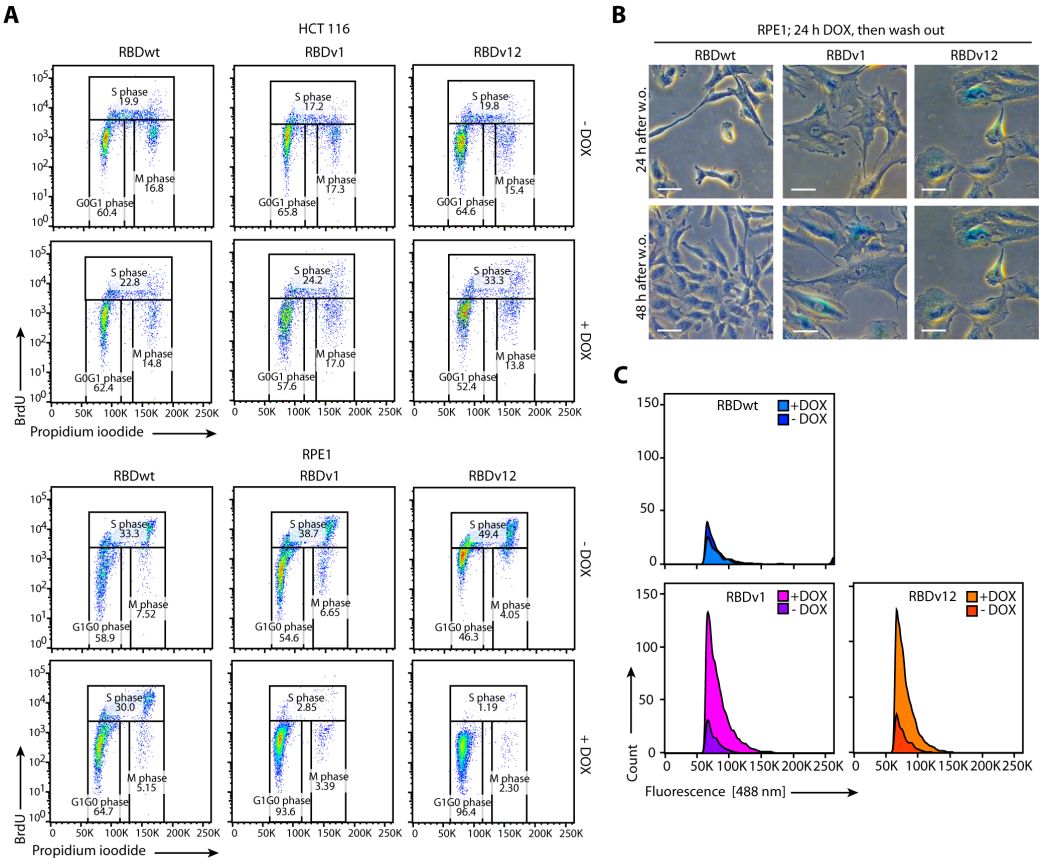

Supplementary Fig. 5. RPE1 cells show cell cycle arrest in the presence of RBDvs and stay senescent after wash out of RBDvs. (**A**) Representative analysis of HCT 116 and RPE1 cells stably transduced with lentivirus encoding HA-tagged RBDwt, RBDv1 and RBDv12 in absence (-DOX) or presence (+DOX) of DOX (1 µg/ml, 72 h). Cells were assayed by flow cytometry for incorporation of 5-bromo-2'-deoxyuridine (BrdU) and propidium iodide (PI). Gated cell populations correspond to S-, G0/G1- and M-phase. (**B**) Bright field microscopy images of transduced RPE1 cells expressing HA-tagged RBDwt or RBDvs upon DOX induction (1 µg/ml, 24 h). Cells were stained for senescence-associated β-galactosidase (SA-β-Gal) activity after 24 or 48 h of doxycycline wash out (w.o.). Scale bars: 50 µM. (**C**) Representative flow cytometry analysis of transduced RPE1 cells expressing HA-tagged RBDwt (blue), RBDv1 (magenta) or RBDv12 (orange) upon DOX induction (1 µg/ml, 48 h) stained for SA-β-Gal activity.

Supplementary Fig. 6

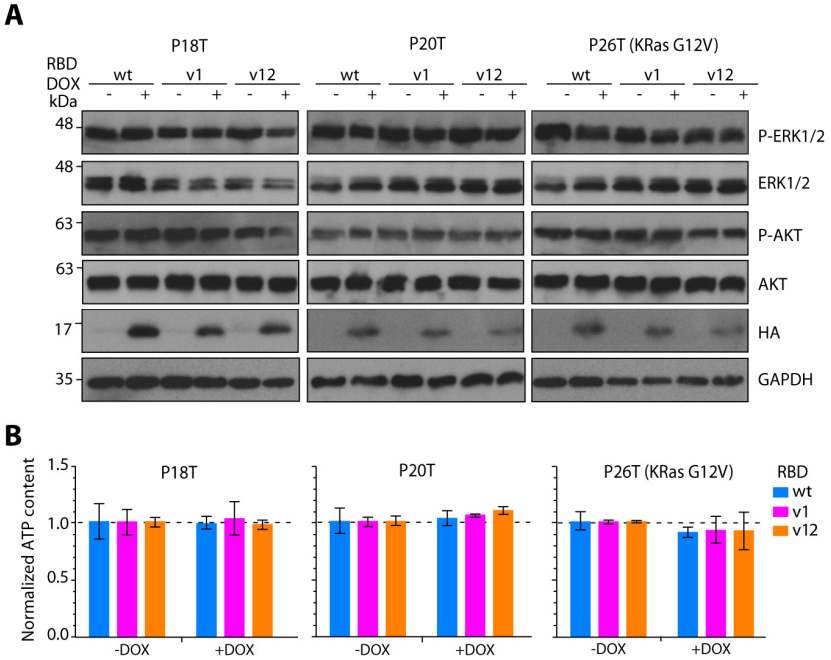

Supplementary Fig. 6. Patient-derived colorectal cancer (CRC) organoids that were insensitive to RBDvs expression. (**A**) Immunoblot of whole cell lysates derived from indicated patient-derived CRC organoids stably transduced with lentivirus encoding HA-tagged RBDwt, RBDv1 and RBDv12 in absence (-) or presence (+) of DOX (2 µg/ml, 72 h). Cell lysates were analyzed using indicated antibodies. (**B**) Cellular ATP content of organoid cultures used in (A) expressing RBDwt (blue), RBDv1 (magenta) and RBDv12 (orange) was measured in a luciferase mediated bioluminescence assay. Reduction of cellular ATP in presence of RBDvs (+DOX) was monitored after 72 h induction and normalized to the luminescence of non-induced control organoids (-DOX) (2 µg/ml, 72 h). Error bars correspond to ± SD of three technical replicates (n=3).

Supplementary Table 1: X-Ray data collection and refinement statistics.

	HRas G12V:RBDv1	HRas G12V:RBDv12
Data collection		
Space group	P 63 2 2	P 63 2 2
Cell dimensions		
a, *b*, *c* (Å)	91.62, 91.62, 151.41	91.76, 91.76, 151.59
α, β, γ (°)	90, 90, 120	90, 90 ,120
Resolution (Å)	151.4 - 2.9 (3.08 - 2.9)	79.47 – 3.1 (3.31 – 3.1)
R_{meas}	0.14 (10.1)	0.15 (5.31)
$CC_{1/2}$	99.9 (42.3)	99.8 (43.9)
$I / \sigma I$	15.1 (0.4)	11.0 (0.44)
Completeness (%)	99.8 (98.7)	97.9 (90.0)
Redundancy	18.0 (18.7)	12.3 (12.6)
Refinement		
Resolution (Å)	2.9	3.1
R_{work} / R_{free}	22.1 / 25.9	23.8 / 26.8
No. atoms		
Protein	1779	1787
Ligand/ion	39	39
Water	8	1
B-factors		
Protein	136.2	145.7
Ligand/ion	112.0	139.0
Water	100.0	109.3
R.m.s. deviations		
Bond lengths (Å)	0.006	0.0086
Bond angles (°)	1.384	1.5068
Ramachandran statistics		
Residue in favoured regions (%)	96	96.1
Residue in allowed regions (%)	4.0	3.5
Residue in disallowed regions (%)	0	0.4

Supplementary Table 2: Dataset from co-immunoprecipitation and mass spectrometry analysis.

Supplementary Table 3: **Patient-derived colorectal cancer (CRC) organoids used in this study and growth response to RBDvs expression.**

HUB tumor organoid*	Viability reduction upon RBDvs expression	Normalized ATP levels measured by cell titer glo after induction with DOX			Published mutational status*			
		RBDwt	RBDv1	RBDv12	KRas	NRas	BRAF	PI3K
P6T	+	0.99 ± 0.01	0.34 ± 0.04	0.44 ± 0.03	G12C	wt	wt	wt
P17T	+	1.09 ± 0.07	0.30 ± 0.01	0.43 ± 0.01	wt	wt	wt	wt
P18T	-	0.98 ± 0.05	1.03 ± 0.12	0.97 ± 0.03	wt	wt	wt	wt
P20T	-	1.32 ± 0.07	1.13 ± 0.07	1.24 ± 0.04	wt	wt	wt	wt
P24bT (MSI)	+	1.07 ± 0.01	0.15 ± 0.02	0.38 ± 0.08	wt	wt	wt	wt
P26T	-	0.90 ± 0.04	0.93 ± 0.09	0.92 ± 0.13	G12V	wt	wt	wt
P28T	+	0.91 ± 0.08	0.42 ± 0.15	0.42 ± 0.10	G12V	wt	wt	wt

*van de Wetering *et al*., 2015
P: patient; T: tumor; MSI: microsatellite instability

Supplementary References:

32. Kunkel TA. Rapid and efficient site-specific mutagenesis without phenotypic selection. *Proc Natl Acad Sci U S A* **82**, 488-492 (1985).

33. Fellouse FA, Sidhu, S.S. Making antibodies in bacteria. In: *Making and using antibodies (G. C. Howard & M. R. Kaser, Eds.)* (ed^(eds). CRC Press, Boca Raton, FL (2007).

34. Kabsch W. Xds. *Acta Crystallogr D Biol Crystallogr* **66**, 125-132 (2010).

35. McCoy AJ, Grosse-Kunstleve RW, Adams PD, Winn MD, Storoni LC, Read RJ. Phaser crystallographic software. *J Appl Crystallogr* **40**, 658-674 (2007).

36. Emsley P, Cowtan K. Coot: model-building tools for molecular graphics. *Acta Crystallogr D Biol Crystallogr* **60**, 2126-2132 (2004).

37. Kovalevskiy O, Nicholls RA, Murshudov GN. Automated refinement of macromolecular structures at low resolution using prior information. *Acta Crystallogr D Struct Biol* **72**, 1149-1161 (2016).

38. Murshudov GN, Vagin AA, Dodson EJ. Refinement of macromolecular structures by the maximum-likelihood method. *Acta Crystallogr D Biol Crystallogr* **53**, 240-255 (1997).

39. Winn MD*, et al.* Overview of the CCP4 suite and current developments. *Acta Crystallogr D Biol Crystallogr* **67**, 235-242 (2011).

40. Tiscornia G, Singer O, Verma IM. Production and purification of lentiviral vectors. *Nat Protoc* **1**, 241-245 (2006).

41. Shevchenko A, Tomas H, Havlis J, Olsen JV, Mann M. In-gel digestion for mass spectrometric characterization of proteins and proteomes. *Nat Protoc* **1**, 2856-2860 (2006).

42. Rappsilber J, Ishihama Y, Mann M. Stop and go extraction tips for matrix-assisted laser desorption/ionization, nanoelectrospray, and LC/MS sample pretreatment in proteomics. *Anal Chem* **75**, 663-670 (2003).

43. Michalski A*, et al.* Mass spectrometry-based proteomics using Q Exactive, a high-performance benchtop quadrupole Orbitrap mass spectrometer. *Mol Cell Proteomics* **10**, M111 011015 (2011).

44. Cox J, Mann M. MaxQuant enables high peptide identification rates, individualized p.p.b.-range mass accuracies and proteome-wide protein quantification. *Nat Biotechnol* **26**, 1367-1372 (2008).

45. Cox J, Neuhauser N, Michalski A, Scheltema RA, Olsen JV, Mann M. Andromeda: a peptide search engine integrated into the MaxQuant environment. *J Proteome Res* **10**, 1794-1805 (2011).

46. Cox J, Hein MY, Luber CA, Paron I, Nagaraj N, Mann M. Accurate proteome-wide label-free quantification by delayed normalization and maximal peptide ratio extraction, termed MaxLFQ. *Mol Cell Proteomics* **13**, 2513-2526 (2014).

47. Tyanova S*, et al.* The Perseus computational platform for comprehensive analysis of (prote)omics data. *Nat Methods* **13**, 731-740 (2016).

48. Terry NH, White RA. Flow cytometry after bromodeoxyuridine labeling to measure S and G2+M phase durations plus doubling times in vitro and in vivo. *Nat Protoc* **1**, 859-869 (2006).

49. Sato T*, et al.* Long-term expansion of epithelial organoids from human colon, adenoma, adenocarcinoma, and Barrett's epithelium. *Gastroenterology* **141**, 1762-1772 (2011).

50. Koo BK*, et al.* Controlled gene expression in primary Lgr5 organoid cultures. *Nat Methods* **9**, 81-83 (2011).